


Atmospheric ice nucleation by macromolecules: Investigating the role of surfactants and micelles

Master Thesis

Author(s):

Miller, Anna J. 

Publication date:

2020-12

Permanent link:

<https://doi.org/10.3929/ethz-b-000682198>

Rights / license:

[Creative Commons Attribution 4.0 International](#)

Atmospheric ice nucleation by macromolecules: Investigating the role of surfactants and micelles

Anna J. Miller

(18-940-403)

Master Thesis

Department of Environmental Science, ETH Zurich

December 21, 2020

Supervisor: Dr. Nadine Borduas-Dedekind

Institute of Biogeochemistry and Pollutant Dynamics

& Institute for Atmospheric and Climate Science

Co-Supervisor: Dr. Claudia Marcolli

Institute for Atmospheric and Climate Science

Abstract

Aerosol-cloud interactions are one of the largest sources of uncertainty in climate predictions. The process of ice nucleation in clouds by aerosols containing ice nucleating macromolecules (INMs) is particularly challenging to predict due to the heterogeneity and complexity of INMs. One quality of macromolecules that may influence their ice nucleating activity is their aggregation behavior and supramolecular structure, yet this relationship remains under-investigated in the context of atmospheric ice nucleation. In this thesis, I explored the effects of aggregation of three micelle-forming surfactants, namely sodium dodecyl sulfate (SDS), sodium deoxycholate, and Triton X-100, and the biopolymer lignin on ice nucleation in droplets. The critical micelle concentration (CMC) was measured for SDS, deoxycholate, and Triton X using three techniques, specifically pyrene fluorescence, conductivity, and dynamic light scattering (DLS). Experimentally measured CMCs were generally found to agree with literature values. However, a CMC could not be found for lignin using these methods, suggesting the absence of micelles in lignin solutions. DLS was additionally used to measure sizes of aggregates in solutions of the four compounds; SDS, deoxycholate, and Triton X had micelles sizes of approximately 4.68 ± 0.09 nm, 2.10 ± 0.06 nm, and 10.0 ± 0.1 nm, respectively. SDS, deoxycholate, and lignin also showed presence of larger aggregates around 100 nm, but Triton X did not. Finally, ice nucleation activity was measured with the Freezing Ice Nuclei Counter (FINC) and revealed that SDS and deoxycholate solutions froze at temperatures above the background only for concentrations higher than the CMC. Moreover, lignin solutions were ice-active at all concentrations although the freezing behavior was non-linear with increasing concentration. Triton X solutions did not nucleate ice warmer than background freezing in FINC. To explain these results, I hypothesize that the secondary aggregates may have an essential role in causing increased freezing temperatures, because Triton X was the only compound not to show secondary aggregates in the DLS measurements. However, all results reported in this thesis remain preliminary. Replicates of DLS and freezing experiments are required to strengthen the suggested trends. Other further research could include analyzing a more extensive set of surfactants and complex organic molecules, as well as investigating mixed-surfactant systems to relate the results to real atmospheric aerosol better. The questions addressed and raised in this thesis can help further the community's understanding of ice nucleation in cloud droplets by organic matter.

Contents

1	Introduction	1
1.1	Atmospheric ice nucleation	1
1.1.1	Ice nucleation of organic matter	1
1.2	Surfactants in atmospheric aerosol	2
1.3	Surfactants and micelles	3
1.3.1	Techniques for characterizing surfactants and micelles	4
1.4	Goals of this thesis	9
2	Methods	9
2.1	Chemicals	9
2.1.1	Standard surfactants	9
2.1.2	Lignin	10
2.2	Sample Preparation	11
2.2.1	Tests to determine best method of sample preparation	11
2.3	Ice nucleation experiments with Freezing Ice Nuclei Counter (FINC)	11
2.4	Micelle probing experiments	13
2.4.1	Pyrene fluorescence 1:3 method	13
2.4.2	Conductivity	13
2.4.3	Dynamic light scattering (DLS)	13
3	Results	14
3.1	Pyrene fluorescence experiments	14
3.2	Conductivity experiments	17
3.2.1	Temperature dependence of SDS micelle formation	17
3.3	DLS experiments	19
3.3.1	Triton X micelle size and CMC	19
3.3.2	SDS micelle size and CMC	20
3.3.3	Deoxycholate micelle size	22
3.3.4	Lignin aggregation sizes	22
3.4	Ice nucleation	24
3.4.1	Trends in freezing temperatures	24
3.4.2	Ice nucleating activity normalized to carbon concentration	27
4	Discussion	29
5	Atmospheric Implications	30
6	Outlook	31
7	Acknowledgements	32
8	References	33
9	Appendix	42

1 Introduction

1.1 Atmospheric ice nucleation

A significant component of the uncertainty in predicting Earth's climate is aerosols' effect on clouds (IPCC, 2013). In particular, some aerosols contain ice nucleating particles (INPs) which cause the freezing of supercooled cloud droplets. Ice crystal concentrations in clouds influence cloud radiative properties, including cloud lifetime and albedo (Storelvmo, 2017). Further, the ice phase is a primary initiator of precipitation; Heymsfield et al. (2020) recently estimated that around 63% of global precipitation originates from the ice phase. Precipitation is then another processes affecting clouds' radiative properties as well as more directly affecting climate. However, it remains a challenge to accurately measure or predict the number of ice crystals in clouds because of the complexity of the freezing process.

Freezing of liquid cloud droplets can occur spontaneously (<1 s) either homogeneously at around -38 °C for a $10\text{ }\mu\text{m}$ droplet or at nearly any warmer temperature by heterogeneous nucleation via INPs (Kanji et al., 2017). Following primary ice formation in a cloud, secondary ice processes can dramatically increase ice crystal formation, thereby further affecting cloud radiative balance (e.g., Lauber et al., 2018; Mignani et al., 2019). Despite the importance of INPs, they are rare – only an estimated 1 in 10^6 particles in the atmosphere are ice nucleating at -20 °C (DeMott et al., 2010) – and after decades of research, a complete mechanistic understanding of heterogeneous ice nucleation is still lacking. The unanswered questions include which substances are effective INPs, and why, when, and how these substances nucleate ice. In this thesis, I attempt to help tackle these questions, specifically regarding the ice nucleation of organic surfactant molecules.

1.1.1 Ice nucleation of organic matter

Though INPs traditionally include solid surfaces such as mineral dusts and whole-cell organisms for which ice can template on the surface of, recent work has found nano-scale ice nucleating macromolecules (INMs) as well (e.g., Pummer et al., 2012; O'Sullivan et al., 2015; Pummer et al., 2015; Mochizuki et al., 2017; Borduas-Dedekind et al., 2019; Bogler & Borduas-Dedekind, 2020; Miller et al., 2020). Some of the first evidence for INMs was of proteins, such as the protein from the highly efficient ice nucleating bacteria *P. syringae* (Maki et al., 1974; Govindarajan & Lindow, 1988; Schmid et al., 1997; Morris et al., 2004). Others have since identified proteinaceous INMs from other bacteria, fungus, soil, and freshwater (e.g., Gurian-Sherman & Lindow, 1993; O'Sullivan et al., 2015; Pummer et al., 2015; Hill et al., 2016; Knackstedt et al., 2018; Suski et al., 2018). In addition, known anti-freeze proteins have been found to be ice nucleating (P. W. Wilson et al., 2010; Qiu et al., 2017; Hudait et al., 2018; Eickhoff et al., 2019). Proteins are useful INMs to investigate mechanistically because of their often well-defined structure and function.

Other organic, non-proteinaceous INMs have also been identified in recent years. For example, INMs, likely carbohydrates, were identified in the washwater of birch pollen by Pummer et al. (2012), Augustin et al. (2013), and Dreischmeier et al. (2017). Similarly, macromolecular and nano-scale ice nucleating activity has been detected in sea spray aerosol (e.g., T. W. Wilson et al., 2015; DeMott et al., 2018; Perkins et al., 2020), freshwater river and lake dissolved organic matter (DOM) (Knackstedt et al., 2018; Moffett et al., 2018; Borduas-Dedekind et al., 2019), and in soils (e.g., Hill et al., 2016; Suski et al., 2018). More recently, lignin, an environmentally-abundant macromolecular biopolymer from woody plants, has been shown to be ice nucleating (Steinke et al., 2019; Bogler & Borduas-Dedekind, 2020; Miller et al., 2020).

Thus, there is ample evidence for the ice nucleating ability of biological and organic macromolecules, but a unifying mechanism for ice-nucleating macromolecules remains elusive.

Much of the theory explaining the “why” and “how” of heterogeneous ice nucleation by biogenic and organic matter stems from the more well-established theory for mineral dust INPs, namely that a surface is needed as a template to order water molecules into the ice structure. One significant factor that allows particles or macromolecules to be ice nucleating is size, as a larger size gives a larger surface. Indeed, it has been shown that larger sizes of proteins or protein clusters (e.g., Mueller et al., 1990; Pummer et al., 2015; Eickhoff et al., 2019; Qiu et al., 2019; Cascajo-Castresana et al., 2020) and longer chains of alcohols (Popovitz-Biro et al., 1994; Ogawa et al., 2009; Qiu et al., 2017) are more efficient ice nuclei. Another recognized factor for a good ice nuclei is its structural match (or mismatch) to the ice lattice; a better match to the ice crystal structure leads to more efficient, or warmer, freezing (e.g., Popovitz-Biro et al., 1994; Qiu et al., 2017). Similarly, the charges and functional groups on the surface of a particle or a macromolecule aid in ordering the water molecules, especially if these functional groups can participate in hydrogen bonding (e.g., OH groups) (e.g., Pummer et al., 2015; Glatz & Sarupria, 2016; Abdelmonem et al., 2017; Qiu et al., 2017; Glatz & Sarupria, 2018; Xue et al., 2019). Still, there is difficulty predicting ice nucleating activity of any given organic substance or macromolecule because of the interplay of these, and likely other, factors. Looking into the ice nucleating ability of surfactants, which are a special class of organic substances that form predictable aggregation structures (*micelles*), may provide a useful view into one aspect of INM mechanisms, namely that of the role of supramolecular structure and size.

1.2 Surfactants in atmospheric aerosol

Surfactants are one of the most versatile substances in the chemical industry, used in products such as detergents, pharmaceuticals, cosmetics, motor oils, paints and inks, and biotechnology (Rosen & Kunjappu, 2012). Surfactants are also naturally occurring; for example, phospholipids are the basis of cell membranes, and fatty acids are produced from cell membrane breakdown (Cochran et al., 2016). It is of no surprise then that both synthetic and biogenic surfactants are present in the environment, and also in atmospheric aerosol. In fact, several researchers over the years have demonstrated the presence of surface-active agents in real atmospheric aerosol (Latif & Brimblecombe, 2004; Kiss et al., 2005; Taraniuk et al., 2007; Asa-Awuku et al., 2008; Baduel et al., 2012; Frka et al., 2012; Cochran et al., 2016; Gérard et al., 2016; Frossard et al., 2019; Gérard et al., 2019; Sugo et al., 2019). Others have investigated the role of surfactants in changing the physicochemical properties of atmospheric aerosol, such as Tabazadeh (2005) and Pfrang et al. (2017). Particularly interesting is the work of Pfrang et al. (2017) which reported spectroscopically-determined complex three-dimensional self-assembly of surfactants in model aerosols, demonstrating micelle formation in micro-scale droplets.

The connection between surfactants in aerosol and their effect on cloud droplet formation has also been investigated (Asa-Awuku et al., 2008; Sareen et al., 2013; Nozière et al., 2014; Petters & Petters, 2016; Ovadnevaite et al., 2017; Forestieri et al., 2018; Kroflič et al., 2018; Lin et al., 2020). However, there is yet to be an effort to assess the effect of surfactants on atmospheric ice nucleation within aqueous aerosol. Some work has investigated the ice nucleation effects of fatty acid and fatty alcohol films and monolayers on aerosol drop surfaces (DeMott et al., 2018; Perkins et al., 2020), though films are of a different phase than dissolved or micellar surfactant solutions. If surfactant concentrations are high enough, the surfactant molecules will not only be on the surface. They will also start to form micelles within the droplet, as Pfrang et al. (2017) demonstrated, and these micelles may aid in ice nucleation. There is one such paper by Kuwabara et al. (2014) which assessed the ice nucleating ability of a series of surfactants

in solution mixed with two other known INPs, a bacteria and silver iodide, and unintentionally found that many of the surfactants were capable of ice nucleation on their own. Together, these studies provide compelling motivation to investigate the ice nucleating ability of surfactants and to probe the relationship between ice nucleating ability and self-assembled supramolecular structure.

1.3 Surfactants and micelles

Surfactants, so-called “*surface-active agents*,” are substances that, at low concentrations, significantly alter the interfacial free energies of a system by adsorbing to the interfaces (Rosen & Kunjappu, 2012). In other words, for an air-water system, a surfactant in the aqueous phase will preferentially arrange at the surface and lower the surface tension of water. Surfactants behave in this way because of their amphiphilic molecular structure. Amphiphilic molecules consist of a hydrophobic group, repellent to water, and a hydrophilic group, attracted to water; typically these are called a polar “head” and a nonpolar “tail” (Fig. 1) (Nesměrák & Němcová, 2006). However, the tail is not always a straight-chain alkyl group, but can also consist of branched alkyl groups, cyclic alkyls, aromatic rings, polysiloxanes, perfluoroalkyl groups, and more (Rosen & Kunjappu, 2012). The hydrophobic group distorts the structure of water by interfering with hydrogen bonding, so the molecules are expelled to the surface to minimize the disruption. The hydrophilic groups, however, prevent the surfactant molecules from forming their own separate phase (as, for example, oil behaves when mixed with water) (Rosen & Kunjappu, 2012). Therefore, the surfactant molecules orient themselves on the surface with their nonpolar groups up toward the essentially nonpolar air, which increases the similarity between the liquid and air phases, thus reducing the surface tension (Rosen & Kunjappu, 2012).

Surfactant molecules also tend to form micelles, or regularly-shaped clusters of molecules in solution, at a certain concentration (Rosen & Kunjappu, 2012). After the amphiphilic surfactant molecules saturate the interface, the bulk-solution molecules begin to associate with each other, minimizing exposure of the hydrophobic moieties to water. They thus form micelles, with the hydrophilic tail directed outward toward the water and the hydrophobic head on the interior (Fig. 1) (Nesměrák & Němcová, 2006; Rosen & Kunjappu, 2012). The concentration at which micelles start to form is termed the critical micelle concentration, or CMC (Fig. 1). The CMC is defined by IUPAC (1997) as the “relatively small range of concentrations separating the limit below which virtually no micelles are detected and the limit above which virtually all additional surfactant molecules form micelles.” The CMC is thus operationally defined with the method of choice, where the measured property is characteristically different below and above the CMC (IUPAC, 1997) (see also Section 1.3.1). The value of the CMC is unique to every micelle-forming surfactant and depends on molecular structure, solvent properties, temperature, and the presence of other substances (Nesměrák & Němcová, 2006; Rosen & Kunjappu, 2012). Additionally, above the CMC, increases in concentration and temperature changes may cause changes in the size and shape of the micelle. The micelle shapes may vary from spherical to rod-like, disk-like, and lamellar shapes with increasing concentration, and the micelles may further aggregate into larger secondary or tertiary aggregates (Rosen & Kunjappu, 2012).

Though micelle-forming compounds are typically the only types of compounds to be considered as surfactants, there are also many other compounds that lower the surface tension of water. In fact, nearly any water soluble organic substance interferes with water’s hydrogen bonding, which is responsible for water’s high surface tension. This interference is evident when measuring the surface tension of organic solutions of increasing concentration (Gérard et al., 2019). Indeed, considerable research has reported lowered surface tension due to a range of organic compounds, for example, carboxylic acids, fulvic acids,

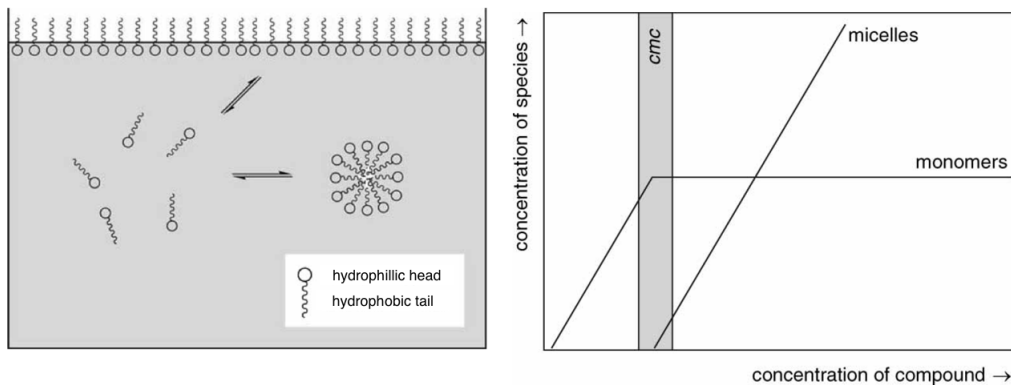


Figure 1: Diagram of the equilibrium between micelles and monomers in solution (left) and the relationship between the concentration of monomers and micelles in solution with increasing total concentration (right). Adapted from Nesměrāk and Němcová (2006).

and humic-like substances (HULIS) (e.g., Guetzloff & Rice, 1994; Kawahigashi & Fujitake, 1998; Kiss et al., 2005; Tabazadeh, 2005; Taraniuk et al., 2007; Tuckermann, 2007; Sugo et al., 2019). These other types of compounds likely do not form micelles, or at least not the regularly shaped and sized micelles as they are traditionally thought of, though this has been debated (e.g., Guetzloff & Rice, 1994; von Wandruszka, 1998; Swift, 1999). Because of the more complex and heterogeneous molecular structures, the formed aggregates are also likely irregular and heterogeneous in size and shape (Wershaw, 1999; Piccolo, 2001; Devarajan et al., 2020).

1.3.1 Techniques for characterizing surfactants and micelles

The study of surfactants has been ongoing for decades, and there are thus many different established methods for characterizing surfactants and measuring their CMCs. The methods for CMC determination can be broadly split into two classes: direct and indirect measurements (Nesměrāk & Němcová, 2006). Direct measurements are those that measure a change of a property of the solution which changes with increasing concentration of the micelle-forming surfactant. A discontinuity of the signal vs. concentration plot gives the CMC (Fig. 2) (Nesměrāk & Němcová, 2006). These methods include measuring surface tension, electrical conductivity, osmotic pressure, and turbidity (Fig. 2). Indirect measurements are those that measure a property of another substance, a probe, in the micelle-forming surfactant solution, where the property of the probe changes with increasing concentration (Nesměrāk & Němcová, 2006). Indirect methods include voltammetric and spectrometric measurements.

The methods used in this thesis for CMC determination include the indirect measurement of pyrene fluorescence (Section 1.2.2.1) and direct measurements of electrical conductivity (Section 1.2.2.2) and dynamic light scattering (Section 1.2.2.3).

1.3.1.1 Pyrene fluorescence 1:3 method

Pyrene is a fluorescent, hydrophobic molecule which is often used to probe micellar systems and to determine the CMC (e.g., Kalyanasundaram & Thomas, 1977; Kalyanasundaram, 1988; Kogej & Škerjanc, 1999; Aguiar et al., 2003; Pan et al., 2008; Kumar et al., 2015; Piñeiro et al., 2015). When a hydrophobic probe like pyrene is transferred from an aqueous environment to a micellar solution, the change in microenvironment around the probe is reflected in a change in its fluorescent intensity. Maximum changes in intensity occur when surfactant concentrations are at or near the CMC (Kalyanasundaram, 1988).

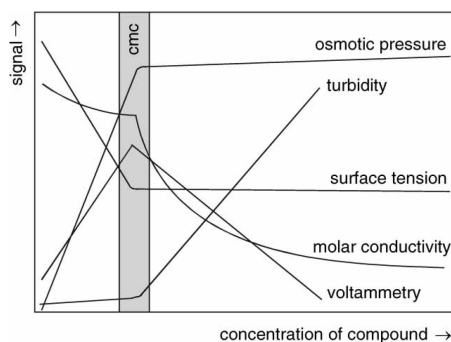


Figure 2: Examples of different methods for measuring the CMC of a compound, and how the signal response for each method changes with concentration. Measurements include osmotic pressure, turbidity, surface tension, molar conductivity, and voltammetry. Reprinted from Nesměrák and Němcová (2006).

Specifically, the “pyrene 1:3 method” utilizes the ratio of fluorescent intensities at pyrene’s first and third vibronic bands of 373 and 384 nm, respectively. A plot of the 1:3 ratio versus surfactant concentration gives a characteristic sigmoidal curve that is used for determining the CMC (Fig. 3). The 1:3 ratio curve below the CMC corresponds to pyrene experiencing a hydrophilic environment. As the surfactant concentration increases, pyrene experiences an increasingly hydrophobic environment, reflected in the 1:3 ratio decreasing in a sigmoidal shape, until above the CMC where the 1:3 ratio stabilizes (Fig. 3). This stabilization at a constant value indicates that the pyrene molecules are completely incorporated into the micelles’ hydrophobic core (Zana et al., 1998; Aguiar et al., 2003). By fitting the curve to a sigmoid function, the CMC can be identified by one of two methods, according to Zana et al. (1998) and Aguiar et al. (2003): 1) for “very low” CMCs (below 1 mM), the inflection point of the sigmoid is taken as the CMC, or 2) for “higher” CMCs (above 1 mM), the CMC is equal to the x-value at the intercept of the line tangent to the inflection point and the line tangent to the constant post-CMC value (Fig. 3) (Aguiar et al., 2003). The reason for the difference is about how steep the sigmoidal decay is, or how quickly pyrene fully partitions to the hydrophobic phase. Zana et al. (1998) explains that low-CMC surfactants have a shallower sigmoidal decrease than high-CMC surfactants, due to a difference in the relative volume of the hydrophobic phase; in low-CMC surfactant systems, a concentration higher than the CMC is required to reach a volume of hydrophobic phase large enough for pyrene to completely partition into, and thus a shallower sigmoidal decrease is observed.

1.3.1.2 Conductivity

Conductivity is a common technique for CMC determination, as it is relatively simple and requires inexpensive instrumentation (Nesměrák & Němcová, 2006). As micelles form in a surfactant solution, the conductivity trend of the solution changes. When conductivity is plotted against total surfactant concentration, there is a change in slope at the CMC (Fig. 4). Obtaining the CMC from the data is, however, not trivial. One simple method is to find the intersection of two linear regressions formed before and after the CMC (Inoue et al., 2007; Perger & Bešter-Rogač, 2007; Kumar et al., 2015). Despite it being one of the more common ways to determine the CMC, this method is less accurate and less reproducible because it is the user’s choice for how many data points to include in the regressions below and above the transition, and it becomes less accurate for compounds with a more gradual transition (Carpena et al., 2002). More quantitatively, one can also calculate the second derivative of the concentration-versus-conductivity data, fit the data to a Gaussian curve, and then take the CMC as the minimum of the Gaussian (Pérez-Rodríguez et al., 1998). Alternatively, Carpena et al. (2002) recommends using the

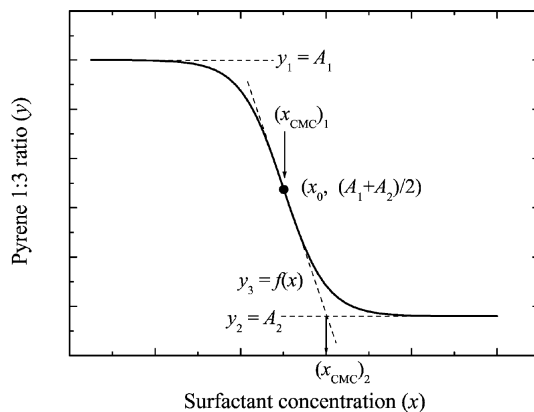


Figure 3: Characteristic decreasing Boltzmann-type sigmoid curve of a pyrene fluorescence experiment, with the pyrene 1:3 ratio plotted versus the surfactant concentration. The two methods of CMC determination, as reported in Aguiar et al. (2003), are represented as $(x_{CMC})_1$, which is the center of the sigmoid, and $(x_{CMC})_2$, which is the intersection of the two straight lines $y_2 = A_2$ and $y_3 = f(x)$. Reprinted from Aguiar et al. (2003).

first derivative, fitting a Boltzmann-type sigmoid curve, and taking the CMC as the center of the sigmoid curve. The various methods result in small but not insignificant differences in the determined CMC, and it is essential to be consistent for comparisons.

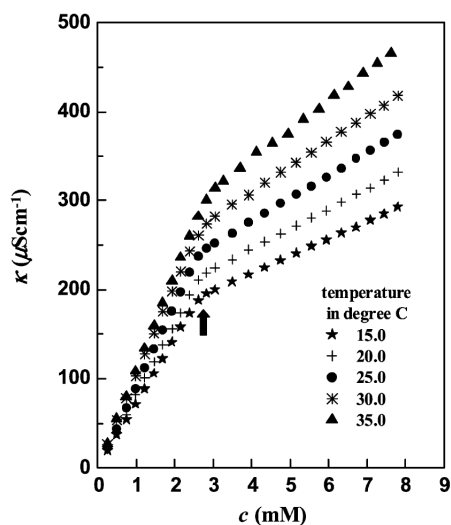


Figure 4: Conductivity K versus concentration c (mM) of a long-chain imidazolium ionic liquid (1-Tetradecyl-3-Methylimidazolium Bromide) at different temperatures, where the change in slope is apparent and occurs at the critical micelle concentration. Reprinted from Inoue et al. (2007).

1.3.1.3 Dynamic light scattering (DLS)

The dynamic light scattering (DLS) technique gives particle size information by measuring the scatter of light from suspended particles diffusing in solution (Hallett, 1994; Berne & Pecora, 2000; Cieřla et al., 2013; Malvern Instruments, 2013). The intensity of light scattered depends on a particle's position, which changes in time due to Brownian diffusion motion. Since Brownian diffusion is size-dependent, a particle size distribution can be obtained from the fluctuation of detected light intensity over time (Fig. 5) (Cieřla et al., 2013; Malvern Instruments, 2013).

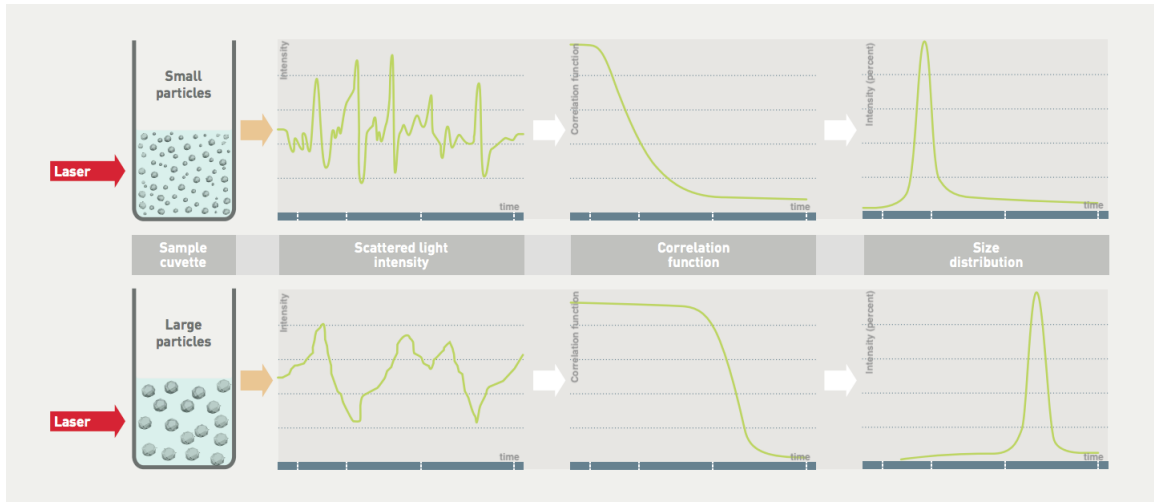


Figure 5: Schematic of the possible data output of a dynamic light scattering (DLS) measurement for small and large particles. The scattered light intensity is measured from an incident laser beam on a suspension in a sample cuvette. The correlation function is based on the scattered light intensity over time, and the size distribution is calculated from the correlation function. Adapted from Malvern Instruments (2020).

The time-dependent fluctuations of intensity are evaluated with an instrument component called a digital correlator, which measures the degree of similarity between two signals over varying time lags (on the scale of nanoseconds to seconds) (Malvern Instruments, 2013). The correlator produces a “correlation function” ($G_2(\tau)$) of the intensity signal, which decreases exponentially with the time lag τ , assuming a monodispersed particle population:

$$G_2(\tau) = A[1 + B * \exp(-2\Gamma\tau)] \quad (1)$$

where A is the time-independent constant, proportional to the squared mean scattered light intensity, B is a coefficient characteristic of the apparatus, and Γ is the speed of the correlation function decay (Cieřla et al., 2013). The speed of the correlation function decay Γ is proportional to the apparent diffusion coefficient D_{app} , described by the equation:

$$\Gamma = D_{app} * q^2 \quad (2)$$

where q is the factor of the scattering vector:

$$q = \frac{4\pi n}{\lambda_0} \sin(\theta/2) \quad (3)$$

where n is the refractive index of the solvent, λ_0 is the length of the laser beam wave in a vacuum, and θ is the angle of the laser (Cieřla et al., 2013). Finally, the apparent diffusion coefficient D_{app} is related to the particle’s apparent hydrodynamic radius $R_{h,app}$ by the Stokes-Einstein equation:

$$D_{app} = \frac{k_B T}{6\pi\eta R_{h,app}} \quad (4)$$

where k_B is the Boltzmann constant, T is the temperature, and η is the solvent viscosity (Cieřla et al., 2013).

When running a DLS measurement, the light intensity per second (or photon count rate) and the correlation function $G_2(\tau)$ are reported graphically in real-time (see for example in Fig. 5). A measurement includes a set number of runs, where a “run” is the set amount of time for which a correlation function is produced. For example, a measurement can have 10 runs of 20 seconds each, where a correlation

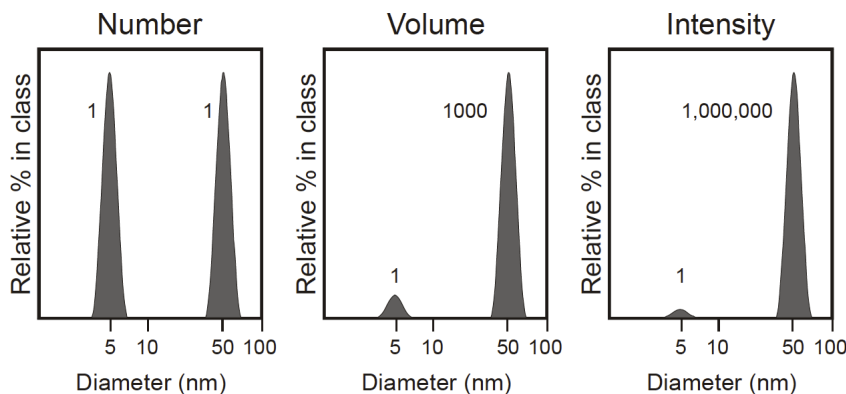


Figure 6: Example of a number, volume, and intensity size distribution with a bimodal particle size population, depicting the favoring of large particle sizes in the intensity distribution. Reprinted from Malvern Instruments (2013)

function is produced with the count rates over every 20 seconds. Then, at the end of the 10 runs, the 10 correlation functions are averaged to give one correlation function. Thus, the output data includes the average correlation function, the average count rate, the average apparent hydrodynamic diameter, and size distributions.

The primary size distribution is an intensity distribution (Fig. 5 and Fig. 6), which is weighted by the scattering intensity of each particle size class. The intensity distribution can be converted to a volume distribution using Mie theory, which can further be converted to a particle number distribution (Fig. 6) (Malvern Instruments, 2013). While the intensity distribution is closest to the raw data, it can appear misleading because it favors the larger sizes, as the relative scattered intensity of a particle is proportional to the particle's diameter to the sixth power (Fig. 6). In contrast, the relative volume of particles is proportional to the particle's diameter to the third power, and the relative number of particles is *not* proportional to the particle's diameter (Fig. 6). It is useful to look at all three size distributions, since they each convey complimentary information. Note, however, that the intensity distribution is technically the most accurate, because the conversion into volume and number distributions hinges on the assumptions that the particle population is made of spherical, homogeneous, and isotropic particles whose optical properties (refraction index and absorbance) are known, and that the correlation function data is of good quality (Malvern Panalytical, 2020). Nevertheless, the size information given from the three distributions can be valuable for comparisons between samples.

Finally, DLS measurements also provide information to estimate the CMC of a surfactant by plotting the change in average count rate over increasing concentration. At concentrations below the CMC, the count rate is low and unchanging, and then increases linearly starting at the CMC (Fig. 7) (Topel et al., 2013; Horiuchi & Winter, 2015).

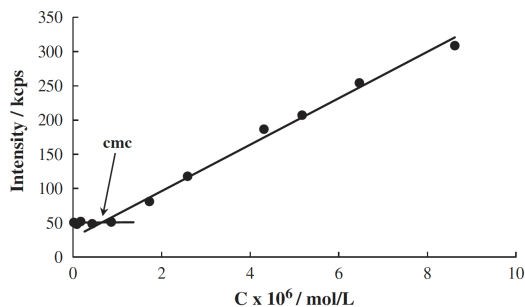


Figure 7: Intensity (average count rate in kilo counts per second, kcps) versus surfactant concentration ($\text{mol/L} * 10^{-6}$) as obtained by DLS measurements for an amphiphilic surfactant, polybutadiene-block-poly(ethylene oxide) diblock copolymer. The CMC is at the point where the intensity starts increasing linearly. Reprinted from Topel et al. (2013).

1.4 Goals of this thesis

Ice nucleation affects clouds and thus climate, but open questions remain on the mechanism of heterogeneous ice nucleation by organic matter. At the same time, surfactants are known components of atmospheric aerosol and there are established methods for characterizing surfactants and their supramolecular properties.

In this thesis, I investigated the role of aggregation and supramolecular structure on ice nucleation. Building on the theories that a surface is required to template ice and that larger sizes are more efficient ice nuclei, I hypothesized that organic molecules that form aggregates can template ice, especially when they aggregate to form large sizes. For example, proteins have been shown to be more ice active in their aggregated cage-like form, which can be induced by pH changes (Cascajo-Castresana et al., 2020). Surfactants that form micelles are thus a useful model to examine aggregation and ice nucleation, and there is limited evidence of how micelle-forming substances potentially present in organic aerosols can act as ice nuclei (Kuwabara et al., 2014). This thesis explores the connection between micellar aggregations and ice nucleation explicitly for the first time. The aggregation properties of three micelle-forming surfactants – sodium dodecyl sulfate, sodium deoxycholate, and Triton X-100 – and the humic-like substance lignin were analyzed with pyrene fluorescence, conductivity, and dynamic light scattering to measure their CMCs and their aggregation sizes. The ice nucleating ability of the four compounds was then measured with an immersion freezing technique, and their freezing behaviors were compared to their micellar properties.

2 Methods

2.1 Chemicals

2.1.1 Standard surfactants

Three common surfactants were studied for their micellar properties and their ice nucleating abilities: sodium dodecyl sulfate (SDS) (Sigma Aldrich, 436143), sodium deoxycholate (Acros Organics, 218591000), and Triton X-100 (Sigma Adlrich, T8787) (Fig. 8). SDS is a synthetic anionic surfactant used in many cleaning and hygiene products, and the CMC is between 6.3 - 8.8 mM at 25°C (Table 1) (Mukerjee & Mysels, 1971). Sodium deoxycholate is the salt of a bile acid and is used as an anionic detergent to solubilize cells. It has a reported CMC of 2.4 - 10 mM at 25°C (Table 1) (Matsuoka & Moroi, 2002). Finally, Triton X-100 is a synthetic nonionic surfactant also used as a detergent in biological appli-

cations, with a CMC of 0.2-0.3 mM at 20-20°C (Table 1) (Zhang et al., 2010; Thakkar et al., 2015; G.-Y. Wang et al., 2017). A range of CMC values is reported because the CMC generally varies depending on which method is used for CMC determination (Mukerjee & Mysels, 1971). Molecular weights reported from their production company were used: 288.38 g/mol for SDS, 414.58 g/mol for deoxycholate, and 625 g/mol for Triton X.

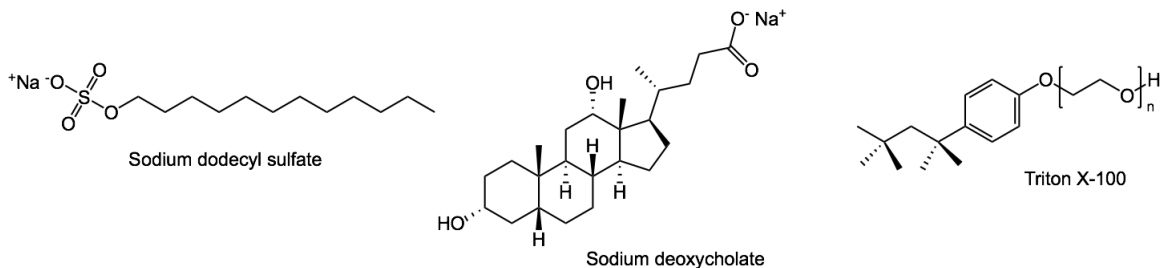


Figure 8: The three standard surfactants studied here. From left to right: sodium dodecyl sulfate (SDS), sodium deoxycholate, and Triton X-100.

Table 1: Literature CMC values of the surfactant compounds used in this thesis.

Compound	CMC at 25°C (mM)	Reference
Sodium dodecyl sulfate (SDS)	6.3 - 8.8	e.g., Mukerjee and Mysels (1971)
Sodium deoxycholate	2.4 - 10	e.g., Jover et al. (1996), Matsuoka and Moroi (2002), Kumar et al. (2015)
Triton X-100	0.15 - 0.37	e.g., Mukerjee and Mysels (1971), Dharaiya and Bahadur (2012), Thakkar et al. (2015)
Lignin	none	

2.1.2 Lignin

In addition to well-characterized surfactants, lignin (low-sulfonate alkali kraft lignin, average molecular weight 10000, Sigma Aldrich, 471003,) was studied in this thesis as a more complex and atmospherically-relevant organic macromolecule. Lignin is a biopolymer (Fig. 9) found in woody plants accounting for about 30% of all organic carbon in the environment (Boerjan et al., 2003). Lignin is a humic-like substance, which are known environmental surfactants (Taraniuk et al., 2007; Tuckermann, 2007; Gérard et al., 2016; Gérard et al., 2019; Sugo et al., 2020). In addition, lignin has previously been shown to be ice nucleation active (Steinke et al., 2019; Bogler & Borduas-Dedekind, 2020; Miller et al., 2020), therefore a good candidate for analysis of correlating surfactant properties to ice nucleation ability.

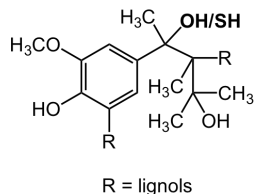


Figure 9: Example molecular structure of lignin.

2.2 Sample Preparation

All solutions were prepared by weighing material into sterile plastic tubes (Eppendorf or Falcon) and diluting with microbiology-free reagent water (Sigma Aldrich, W4502; SA water). All solutions were vortexed and sonicated until complete solubilization (no visible particles remaining in solution) and then left at room temperature overnight or until the foam and bubbles disappeared. For DLS and ice nucleation experiments, solutions were then filtered through a 0.2 μm sterile PES syringe filter (Whatman, GE Healthcare Life Sciences) to remove contaminating dust or other larger particles. For all molecules except lignin, which was previously shown to have stable ice nucleating activity over time (Miller et al., 2020), solutions were prepared no longer than 48 hours before analysis by any of the following methods and were stored at room temperature.

2.2.1 Tests to determine best method of sample preparation

Sample preparation is crucial for ice nucleation experiments, as any small amount of contamination can cause early freezing. A review by Polen et al. (2018) has looked explicitly into water contamination in ice nucleation experiments. My previous work also investigated non-homogeneous freezing behavior in FINC, suggesting possible effects of the tray shape and material (Miller et al., 2020). Here, I evaluated the impact of using glassware versus sterile plastic tubes for sample preparation. Samples prepared in glassware cleaned with 3x water, 3x acetone, and heating to 120°C were shown to have higher ice nucleating activity than samples prepared in sterile plastic tubes (Fig. 10) The glassware may have been contaminated with substances from previous use which was not removed in the cleaning procedure. The plastic tubes, however, are single-use, minimizing sources of contamination. Therefore, I used the plastic tubes for sample preparation and storage.

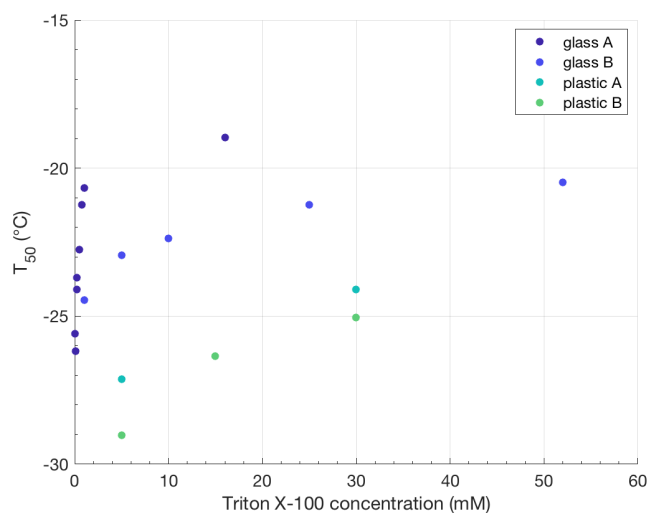


Figure 10: The median freezing temperature (T_{50}) of Triton X solutions of varying concentration and preparation methods. Replicate concentration series in cleaned glassware (purple and dark blue markers) and replicate concentration series in plastic tubes (light blue and green markers) demonstrate the issues of reproducibility.

2.3 Ice nucleation experiments with Freezing Ice Nuclei Counter (FINC)

The home-built drop Freezing Ice Nuclei Counter (FINC) was used to measure the ice nucleating ability of the various surfactant solutions of interest, as described in Miller et al. (2020). FINC uses an ethanol bath to cool microliter-sized sample aliquots to -32°C , while a camera records freezing from above (Fig.

11a,b). In a laminar-flow fumehood to prevent contamination from lab air, samples were pipetted into 96-well Piko PCR plates, pre-cleaned for one hour at 120 °C. The pipetted volume depended on the sample; for samples with very low ice activity (i.e., very near the background limit), larger volumes were required to be able to detect freezing above the background. Here, volumes of 5 μL were used for lignin and SDS, and 10 μL for Triton X and deoxycholate. After preparation, the trays were placed inside the ethanol bath, with a plexiglass cover to prevent contamination during an experiment. The wells in the bath were illuminated from below with an LED-array. The bath was then ramped down from 0 °C to -32 °C at a rate of 1 °C/min while the camera recorded photos every 0.2 °C. At the same time, the ethanol bath level height was continuously kept constant to ensure the wells were always sufficiently submerged; a level sensor measured the height of the bath, and a peristaltic pump was programmed to move ethanol between the bath and an ethanol reservoir (Fig. 11c), to counteract the effect of ethanol density increasing at lower temperatures.

After each experiment, the photographs were analyzed for freezing. The process is based on the principle that frozen water scatters light significantly more than liquid water. For example, a frozen well appears dark compared to an unfrozen well (Fig. 11d). To start the data analysis, a Circular Hough transform algorithm, as described in David et al. (2019), was implemented to locate the wells on the images automatically. When this method failed to select the wells accurately, there was also an option for manual well-alignment. Once the wells were located, the average pixel intensity was calculated per well per image, from which an intensity profile as a function of temperature was generated. Finally, the greatest change in light intensity was attributed to the freezing temperature. The data output for each experiment then was a vector of these 288 freezing temperatures, which could be used for all further analysis and data visualization.

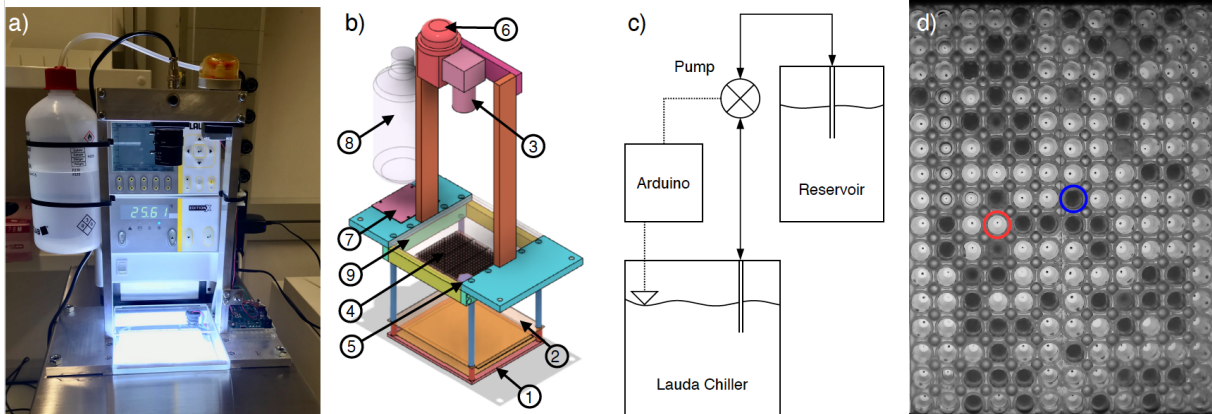


Figure 11: (a) Photograph of FINC. (b) Computer-aided design (CAD) software model of the movable structure placed inside the Lauda bath. The circled numbers correspond to the following components: (1) chip-on-board LED-array, (2) thin polytetrafluoroethylene sheet, (3) camera, (4) three clear Piko™ PCR trays, (5) level sensor, (6) peristaltic pump, (7) Arduino board and stepper motor driver, (8) ethanol reservoir, and (9) Plexiglas plate. (c) Flow chart of the bath leveler control setup. (d) Image of two of the three trays taken by the FINC camera showing the difference in light intensity between the liquid (circled in red) and frozen (circled in blue) wells used for freezing temperature detection. Reprinted from Miller et al. (2020).

2.4 Micelle probing experiments

2.4.1 Pyrene fluorescence 1:3 method

Pyrene fluorescence experiments were performed based on the method by Aguiar et al. (2003). A 100 μM pyrene solution was prepared by weighing 1.0 mg of pyrene into 90:10 acetonitrile:water; the solution was stored in the fridge at 4 $^{\circ}\text{C}$. For each surfactant, a dilution series was prepared, with at least 10 concentrations ranging from below to above the expected CMC from the literature (Table 1); for lignin a concentration series was prepared spanning the range of its solubility in water (up to 2000 mg/L). The pyrene solution was then spiked into the surfactant solutions to obtain a final pyrene concentration of 2 μM . Every sample was gently shaken to ensure complete mixing of the solutes. Finally, 200 μL of each solution was pipetted in triplicates into a black polystyrene 96-well plate (NuncTM F96 MicroWellTM, Thermo Fisher). The prepared trays were covered and brought to the Tecan Infinite[®] 200 PRO Microplate Reader (Tecan, Switzerland) to be analyzed. The fluorescence method on the plate reader used an excitation wavelength of 335 nm and measured fluorescent intensity at 373 and 384 nm. Each well was measured in triplicate, and all measurements were conducted at a set temperature of 29 $^{\circ}\text{C}$. The output data were intensities of both fluorescent wavelengths for each of the replicate excitations of each sample well. For calculating the CMC based on the pyrene 1:3 ratio, the ratio of the intensity at 373 nm to the intensity at 384 nm was calculated and plotted against surfactant concentration, as shown in Figure 3.

2.4.2 Conductivity

Conductivity was measured for SDS, sodium deoxycholate, and lignin. Note that Triton X is nonionic and thus has a conductivity of 0 $\mu\text{S}/\text{cm}$. Measurements were made using an Oakton Waterproof CON 150 portable conductivity meter (Fisher Scientific). The Oakton conductivity meter has a one-point-per-range calibration, a conductivity resolution of 0.01 $\mu\text{S}/\text{cm}$ to 0.1 mS/cm, and an accuracy of $\pm 1\%$. It also measures temperature in the range of -10 to 110 $^{\circ}\text{C}$ with a resolution of 0.1 and an accuracy of $\pm 0.5^{\circ}\text{C}$. For the conductivity experiments, samples were kept at the desired temperature by submerging them inside an ethanol cooling bath while simultaneously stirring by hand with the conductivity probe. To obtain a concentration series for each surfactant, a sample container was first filled with 20 mL of MilliQ water and brought to the desired measurement temperature (25, 15, 10, 5, or 0 $^{\circ}\text{C}$). Then, a small amount (e.g., 100 - 1000 μL depending on the desired final concentration) of a concentrated surfactant solution was added in steps to slowly increase the concentration in the sample container. In between each addition, the sample was stirred, and the conductivity measurement was recorded only when both the temperature and the conductivity reading stabilized, typically after 2-5 minutes. In between each concentration series, the Oakton probe was rinsed with MilliQ water and dried to prevent cross-contamination or unintended dilution. The CMC was obtained through inflection point analysis of the conductivity versus concentration plot.

2.4.3 Dynamic light scattering (DLS)

Dynamic light scattering (DLS) was the final method used to determine the CMC, with the additional ability to measure the size of the micelles or agglomerates. Here, DLS measurements were done with a Malvern Zetasizer Nano SZ (Malvern Panalytical). The measurement range for particle size is 0.3 nm to 10.0 μm in diameter, with an accuracy of $\pm 2\%$ and a precision of $\pm 2\%$. The Zetasizer uses a He-Ne laser at 633 nm and a measurement angle of 173 $^{\circ}$. Using a 173 $^{\circ}$ angle is known as backscatter detection. It is part of a new technology called Non-Invasive Back-Scatter (NIBS), which is advantageous

over the previously common 90° angle because it can be used on higher concentration samples, there is reduced multiple-scattering effects, and there is reduced scattering by larger foreign particles (Malvern Instruments, 2013). All measurements were done at 25 °C. For each sample, three measurements of 10 by 20-second runs were taken to assess the reproducibility and stability (over 200 seconds) of the suspension. The instrument and software automatically determines the best attenuation level to obtain backscatter intensities in the proper range for analysis. The attenuator modifies the laser intensity, and can be set to a level between 1 and 11, where 11 is the maximum attenuation, used for more dilute samples. The attenuation used for each sample was recorded with each measurement.

For CMC and particle size determination, a dilution series of the surfactants of interest were prepared, ranging from below to above the expected CMCs (see Table 1). Directly before analysis in the Zetasizer, samples were pipetted into disposable plastic cuvettes, and then taken out with a syringe and filtered through a 0.22 µm Nylon filter in three cycles to ensure all contamination of larger particles from the cuvette were removed, as these can significantly interfere with the backscatter signal. The highest concentration was then measured first, using the “automatic attenuation” setting to automatically determine the best attenuation level for the sample series. The lower concentrations in the dilution series were then measured with the “manual attenuation” setting, with the attenuator set to the same level as the initial sample, to allow for direct comparison of the count rate between the different concentrations. All measurements were done in triplicate, with each measurement containing 10 runs of 20 seconds each. Finally, the average count rate for each measurement was plotted against the surfactant concentration to obtain the CMC.

The mean particle size of micelles within a sample was obtained from the reported average hydrodynamic diameter and the given size distributions. However, the size information is less reliable for concentrations near or below the CMC because there are too few micelles. Therefore, in addition to the dilution series in the CMC range, a few samples of much higher concentration (e.g., 10 to 100 times higher, depending on solubility limitations) were prepared and measured with “automatic attenuation” to obtain more reproducible and accurate sizes.

3 Results

3.1 Pyrene fluorescence experiments

The pyrene fluorescence 1:3 method was used to measure the CMC of the three known micelle-forming surfactants and of lignin. For SDS, deoxycholate, and Triton X, a sigmoidal curve fit was obtained by plotting the pyrene fluorescence 1:3 ratio versus the surfactant concentration (best examples for each are shown in Fig. 12a, 12b, 12c; results from all measurements are in Appendix Fig. A1, A2, A3). The CMC was determined according to Aguiar et al. (2003), using both $CMC_{method1}$ (CMC as the center of the sigmoid) and $CMC_{method2}$ (CMC as the intersection of two tangent lines on the sigmoid, see Section 1.3.1.1); the values obtained from both analysis methods are reported in Table 2 for each compound. The CMCs of SDS, deoxycholate, and Triton X obtained fit well within the range of CMC values reported in the literature (Table 2). It should be noted again that Aguiar et al. (2003) recommend $CMC_{method1}$ as the most appropriate method for Triton X because the CMC is less than 1 mM, and $CMC_{method2}$ as the most appropriate for SDS and deoxycholate because their CMCs are greater than 1 mM. Indeed for Triton X, $CMC_{method1}$ gives a CMC that more closely fits the literature values.

For lignin, however, the fluorescence of pyrene did not behave as the other surfactants. In fact, the

1:3 ratio versus concentration did not give a decreasing sigmoidal curve, but rather led to an increasing logarithmic curve (example shown in Fig. 12d, two replicate experiments in Appendix Fig. A4). Because a sigmoid cannot be fit to this data, a CMC could not be obtained. To investigate the result further, the pyrene fluorescent intensity at each wavelength over increasing lignin concentration was compared to the same of deoxycholate (Fig. 13). In the deoxycholate concentration series, the fluorescence of pyrene at 384 nm (Peak 3) in water was approximately 2600 Relative Fluorescence Units (RFU). As the concentration of deoxycholate increased and approached the CMC, the pyrene fluorescence remained below 3000 RFU, and subsequently increased logarithmically to 14000 RFU (Fig. 13). However, in the lignin solutions, the fluorescence of pyrene at 384 nm decayed with increasing lignin concentrations to 700 RFU (Fig. 13). This discrepancy might be explained by the interference of lignin with pyrene fluorescence, particularly since lignin absorbs in the wavelength range of the excitation and fluorescent wavelengths (see Appendix Fig. A5). It should also be noted that two control measurements of lignin at 500 mg/L and 1500 mg/L without pyrene showed that lignin itself did not fluoresce (Fig. 13). Three possible explanations for the decreasing fluorescence of pyrene observed in Figure 13 are that 1) the excitation of pyrene molecules is inefficient with increasing lignin concentration because lignin absorbs the incoming photons; 2) pyrene is excited but rather than fluorescing, it transfers its energy to lignin, or 3) pyrene is excited, but the fluoresced photons are absorbed by lignin and do not reach the detector. Any of these scenarios, or a combination thereof, could explain the observed decrease in fluorescence. Further, because of lignin’s interference with pyrene fluorescence, one may not be able to observe micelle formation in these solutions if it were present.

In summary, the pyrene 1:3 method successfully demonstrated micelle formation and allowed for the calculation of the CMC of SDS, deoxycholate, and Triton X. Unfortunately, the method was inappropriate for probing aggregates or possible micelles of lignin due to the likely interference of lignin’s absorbance in the relevant wavelengths.

Table 2: CMC values obtained by the pyrene fluorescence, reported by using either $CMC_{method1}$ and $CMC_{method2}$, with literature values for reference. Average \pm standard deviations of three trials are reported for SDS and deoxycholate, and averages of two trials are reported for Triton X.

Compound	Lit. CMC (mM)	$CMC_{method1}$ (mM)	$CMC_{method2}$ (mM)
SDS	6.3 - 8.8	6.98 ± 0.43	8.04 ± 0.48
Deoxycholate	2.4 - 10	4.20 ± 1.64	7.2 ± 0.3
Triton X	0.15 - 0.37	0.35	0.51
Lignin	None	None	None

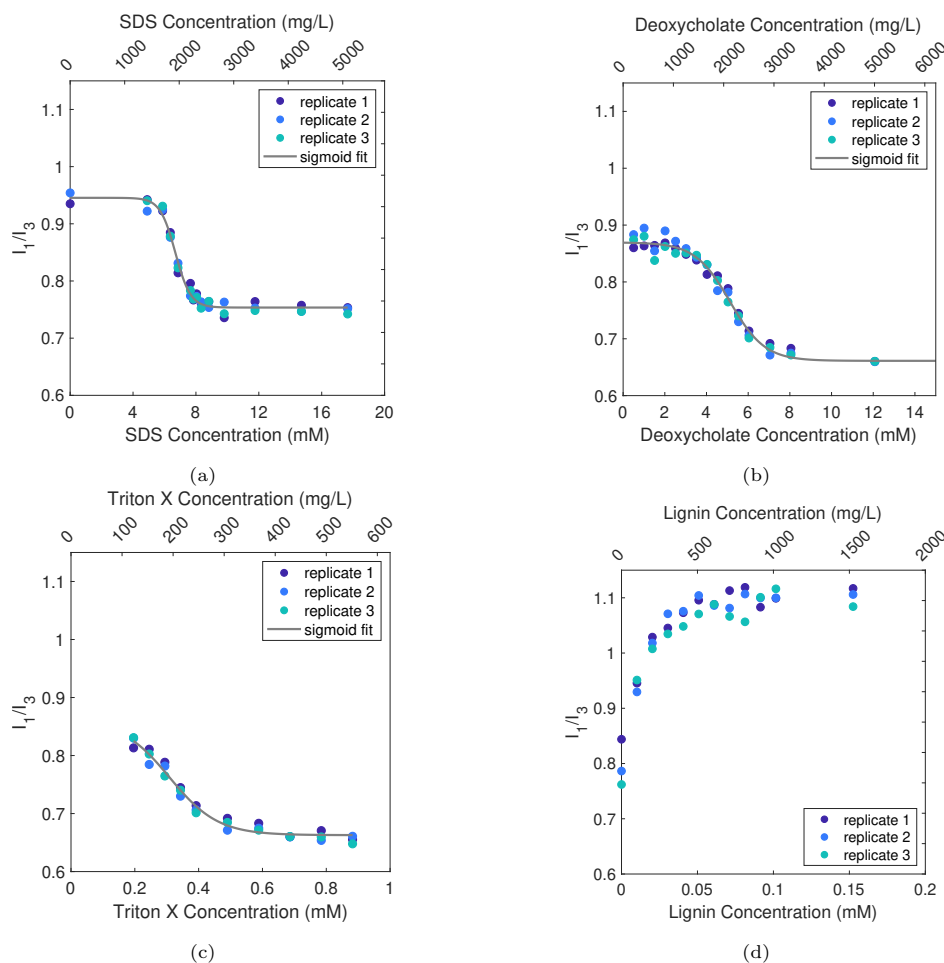


Figure 12: Pyrene fluorescence 1:3 ratio versus concentration for a) SDS, b) deoxycholate, c) Triton X, and d) lignin. The I_1/I_3 ratio (y-axis) is the ratio of fluorescent intensities at 373 and 384 nm wavelengths. Markers indicate experimental values in triplicate at each concentration, and curves are a sigmoid fit through the data (only in a, b, c). Replicates 1, 2, and 3 (dark to light blue) indicate results of identical solutions pipetted into three different wells. Samples at each concentration contain $2\ \mu\text{M}$ pyrene.

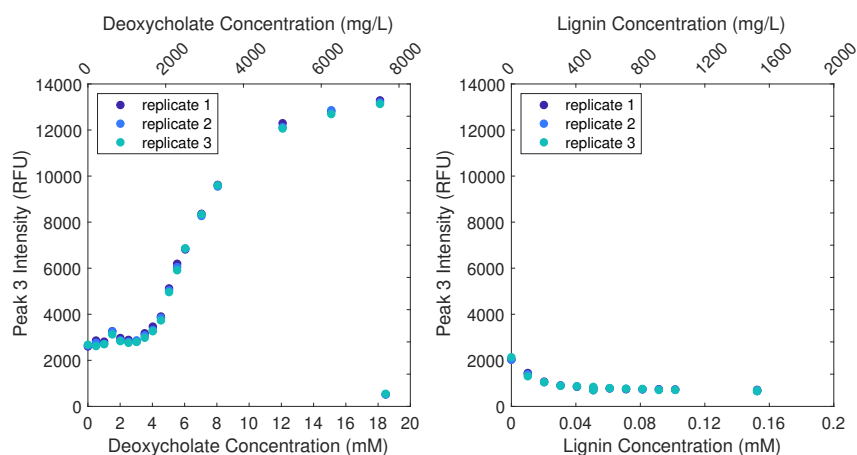


Figure 13: Comparison of the fluorescent intensities (in Relative Fluorescence Units RFU) of Peak 3 at 384 nm versus concentration for deoxycholate (left) and lignin (right). Replicates 1, 2, and 3 (dark to light blue) indicate results of identical solutions pipetted into three different wells. Samples at each concentration contain $2\ \mu\text{M}$ pyrene, except for controls at 18.5 mM deoxycholate and at 500 and 1500 mg/L lignin in which no pyrene was added.

3.2 Conductivity experiments

The second method used to measure the CMC of each compound was conductivity. The electrical conductivity of a concentration series was measured for SDS at 25, 15, 10, 5, and 0 °C (Fig. 14a), for deoxycholate at 25, 15, and 0 °C (Fig. 14b), and for lignin at 25 and 0 °C (Fig. 14c). Triton X is non-ionic and thus its CMC could not be measured using this method. The conductivity method only worked effectively for SDS, and thus further temperature experiments with deoxycholate and lignin were not pursued.

The CMC was determined by fitting a sigmoid curve to the first derivative of conductivity versus concentration (Fig. 14). Other data analysis techniques suggested in the literature were attempted (e.g., fitting a Gaussian to the second derivative as in Pérez-Rodríguez et al. (1998)), but the sigmoidal method was used and deemed most appropriate because of a well-fitting curve. This method was successful in identifying the CMC for SDS (Figure 15a). The CMC values for two trials of SDS at 25 °C were 7.95 and 7.60 mM, in agreement with the range of literature values (Table 2). The CMC values of SDS at the other temperatures measured are reported and discussed in Section 3.2.1.

For deoxycholate, however, the conductivity-concentration data was linear (R^2 range of 0.996 to 1 for all trials and temperatures; Fig. 14b); the first derivative showed an evenly scattered, shapeless distribution (Fig. 15b). Therefore, a CMC could not be determined. The reason for the linear behavior is unclear, as Kumar et al. (2015) for example reported success using the conductivity method to find the CMC for deoxycholate. One plausible explanation that I investigated was the possibility of a kinetic component to micelle formation. I hypothesized that more time between the addition of the surfactant and the conductivity measurement could be needed for the micelles to form. To test this hypothesis, an experiment was performed where the conductivity was measured for five concentrations (0, 3.4, 8.7, 11.1, and 13 mM) and where the solution was left undisturbed for 1 hour following each subsequent surfactant addition. The conductivity was measured before and after 1 hour, rather than after 2-5 minutes as in previous experiments, to test the kinetics of micelle formation. A one hour timespan was chosen because the solutions rested for approximately one hour during the pyrene fluorescent experiments (Section 3.1), where deoxycholate's CMC could be measured. However, after 1 hour, the conductivity did not change. The resulting conductivity-concentration curve was still linear ($R^2 = 0.9997$) and matched the previous experiments (Fig. A6).

The conductivity experiments with lignin also produced linear curves for both trials of both temperatures (the lowest R^2 was 0.9982; Fig. 14c). Therefore, the first derivative plot could not be fitted to a sigmoidal curve (Fig. 15c) and thus a CMC could not be extracted. This result indicates that lignin does not form micelles, which is in agreement with the lack of CMCs reported in the literature (Table 1).

3.2.1 Temperature dependence of SDS micelle formation

Because of my interest in how micelles affect freezing, it was essential to measure the temperature dependence of the CMC of the compounds, especially at colder temperatures. Measuring at different temperatures was possible with the conductivity method, though only until 0 °C because of limitations with supercooling large volumes of water.

The temperature dependence of the CMC of SDS was therefore investigated (Fig. 16a,16b). A partial U-shaped curve was obtained from the data, where the CMC decreased between 0 and 25 °C. Others have previously reported a U-shaped curve for the CMC temperature dependence of SDS (Shah et al., 2001; Kim & Lim, 2004; Noudeh et al., 2007; Marcolongo & Mirenda, 2011; Tennouga et al., 2015),

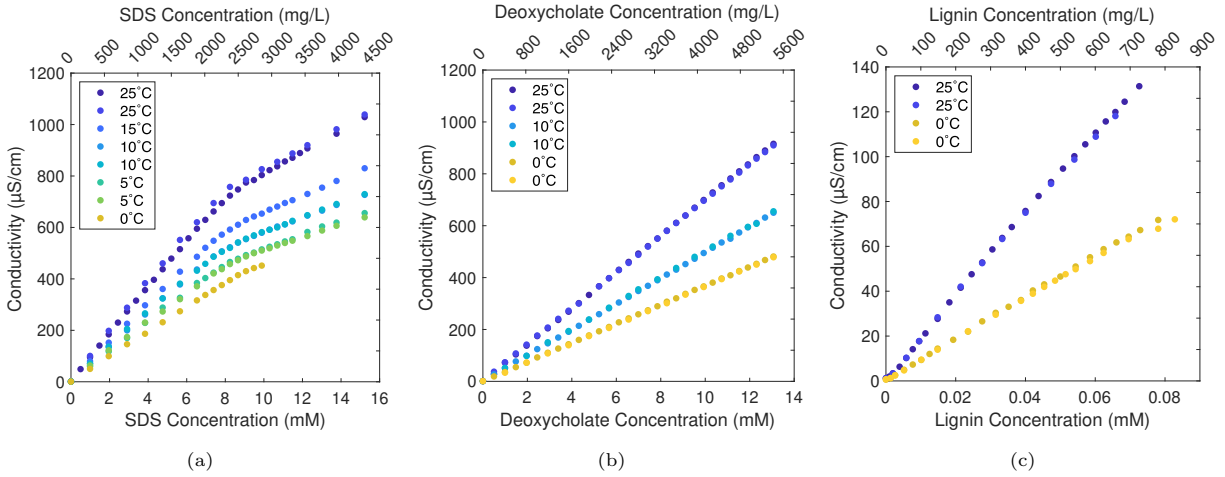


Figure 14: Conductivity versus concentration measurements for a) SDS, b) deoxycholate, and c) lignin. Conductivity was measured for a concentration series at different temperatures: 25 °C (purple markers in a, b, c), 15 °C (blue markers in a), 10 °C (light blue markers in a,b), 5 °C (green markers in a), and 0 °C (yellow markers in a, b, c).

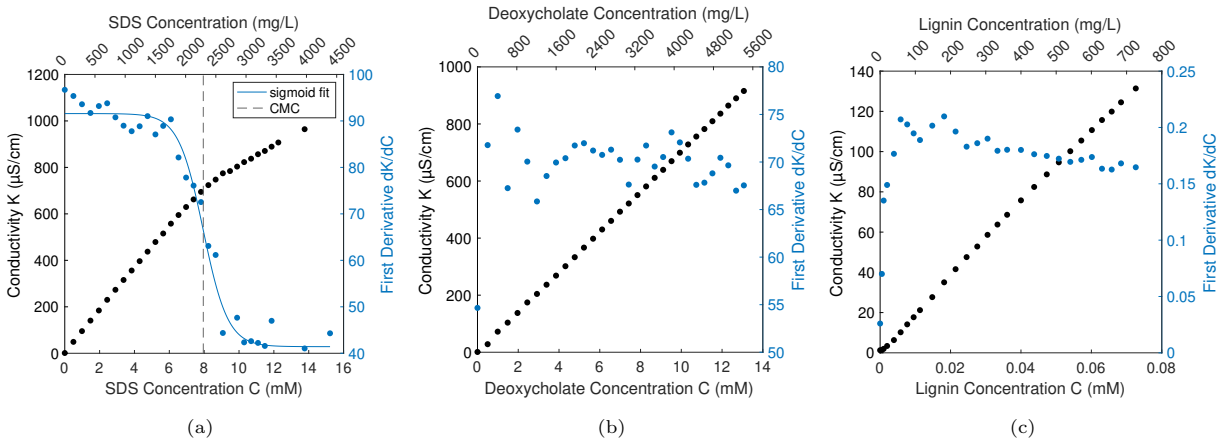


Figure 15: Visualization of the analysis of conductivity measurements to elucidate the CMC for a) SDS, b) deoxycholate, and c) lignin. Black markers indicate conductivity versus concentration data and blue markers indicate the first derivative of conductivity-concentration data. In a), the first derivative was fit with a sigmoidal curve (blue line) and the CMC was taken as the center of the sigmoid (black dashed line).

though others have not measured at 0 °C. As suggested by Kim and Lim (2004), the data was fit with a curve of the form $\ln(CMC) = A + B(T) + C/(T)$ with temperature in Kelvin (Fig. 16b); the coefficient values obtained were $A = -132.1$, $B = 0.2194$, and $C = 18440$. The curve fits reasonably well with my experimental data ($R^2 = 0.8419$). The minimum at $T = 290$ K and $\ln(CMC) = -4.88$ is similar to that of $T = 295$ K, $\ln(CMC) = -4.81$, reported for SDS by Marcolongo and Mirenda (2011).

Unfortunately, the temperature dependence at sub-zero temperatures is still unknown. Based on these experiments, a CMC range of 2 mM between 25 and 0 °C was observed. Though one should interpret with caution, I hypothesize that a CMC change in the range of 2 mM may not affect the CMC-dependent difference observed in the ice nucleation experiments presented in Section 3.4.

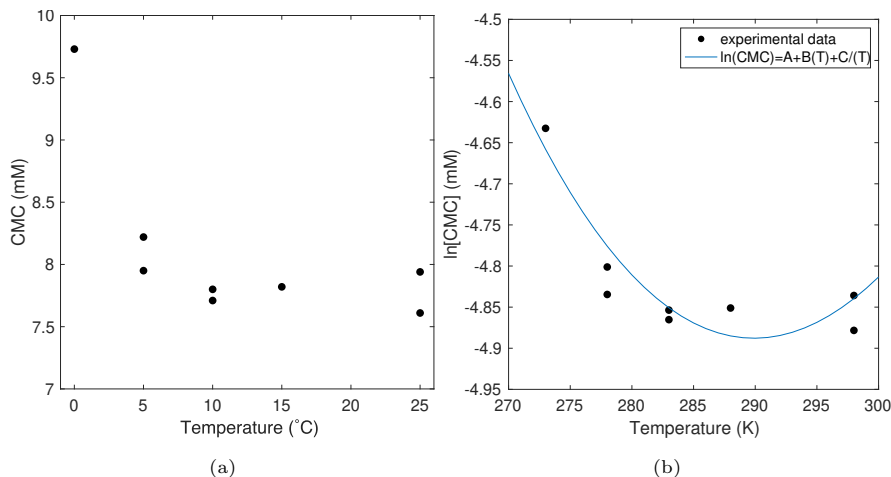


Figure 16: Temperature dependence of the CMC of SDS. a) The CMC of SDS in mM is plotted versus the temperature ($^{\circ}\text{C}$) at which the conductivity experiment was conducted. b) The natural logarithm of the CMC of SDS is plotted versus temperature (K) and a fit of the form $\ln(\text{CMC}) = A + B(T) + C/(T)$, as recommended by Kim and Lim (2004). The coefficients for the curve fit are $A = -132.1$, $B = 0.2194$, $C = 18440$ ($R^2 = 0.8419$).

3.3 DLS experiments

Dynamic light scattering (DLS) was used to measure the CMC and to estimate sizes of Triton X (Section 3.3.1), SDS (Section 3.3.2), deoxycholate (Section 3.3.3), and lignin (Section 3.3.4). For each compound, the correlation functions were used to evaluate the data quality to assess how reliable the results are for CMC and particle size. In general, conditions for good quality correlation functions are a) a correlation function with a y-intercept close to 1, b) reproducible correlation functions at each concentration, and c) a smooth exponential decay (Malvern Instruments, 2013). When these conditions are not met, the interpretation must be made with caution.

3.3.1 Triton X micelle size and CMC

DLS measurements of Triton X were taken for a concentration range near the CMC between 0.1 and 1.0 mM, and additionally at 30 and 100 mM to investigate aggregation at higher concentrations. The conditions for good-quality correlation functions were met for Triton X, especially at concentrations of 100, 30, and 1 mM (Fig. 17a). The correlation functions for 100 and 30 mM were nearly identical, indicating excellent reproducibility of micelle sizes at these concentrations (Fig. 17a). At 1 mM, the correlation function y-intercepts were below 0.8 and were less reproducible between the triplicates, yet still met the data quality controls. More notable was the shift of the 1 mM curve to the right from the 100 and 30 mM curves. The shift to the right indicates that for a longer time lag, there was the same degree of correlation. In other words, particles present in solution were slower-moving and were thus larger. Indeed, this trend of decreasing size with increasing concentration has been reported before for Triton X (Streletzky & Phillies, 1995). However, it is puzzling that this shift to larger sizes was only present between 30 mM and 1 mM. Indeed, below 1 mM, the intercepts of the correlation functions decreased, and the 0.9, 0.8, and 0.7 mM curves shifted slightly to the left (i.e., a smaller time lag for the same degree of correlation) with decreasing concentration, again indicating a slight decrease in size (Fig. 17a). Below 1 mM, however, the correlation functions were of poorer quality, with jagged functions and less reproducibility, and therefore, one should interpret this data with caution. Accordingly, I only report the micelle diameters calculated using the 100, 30, and 1 mM correlation functions. The average

hydrodynamic diameters calculated by the Malvern Zetasizer DLS software for the micelles at 100, 30, and 1 mM are 10.0 ± 0.1 nm, 9.3 ± 0.1 nm, and 34.3 ± 1.2 nm, respectively, with an average \pm standard deviation of triplicates. Li et al. (2000) found that the average hydrodynamic diameter at 6 g/L (equivalent to 9.6 mM) was close to 9 nm at 25 °C on DLS, which agrees well with my result.

In addition to comparing the calculated average hydrodynamic diameter, the intensity size distributions were used for estimating micelle sizes (Fig. 17b; volume and number size distributions in Appendix Fig. A7). For Triton X, the intensity size distributions for 100 and 30 mM showed a single, narrow peak centered around 10 nm, agreeing with the average hydrodynamic diameter. At 1 mM, the size distribution was much broader, with the main peak around 50 nm and a secondary peak at 10 nm. This result also agrees with the larger hydrodynamic diameter reported here for 1 mM. It is unclear whether the shift toward larger sizes was a real result of the micelles being larger than at 30 mM or if it was due to noise because of the lower signal-to-noise ratio of the less concentrated solutions. The size distributions for the concentrations below 1 mM were highly variable, as was their corresponding correlation functions, and therefore should not be interpreted further (Appendix Fig. A7).

Finally, to find the CMC of Triton X from the DLS measurements, the average count rate versus concentration was plotted (Fig. 17c). At the lowest concentrations of Triton X of 0.1 and 0.2 mM, the count rate was very low and steady at 30 kspc, and then began increasing linearly at 0.3 mM. These results indicate that the CMC was between 0.2 and 0.3 mM, which agrees with the literature CMC range for Triton X and the previous pyrene fluorescence measurements (Table 2).

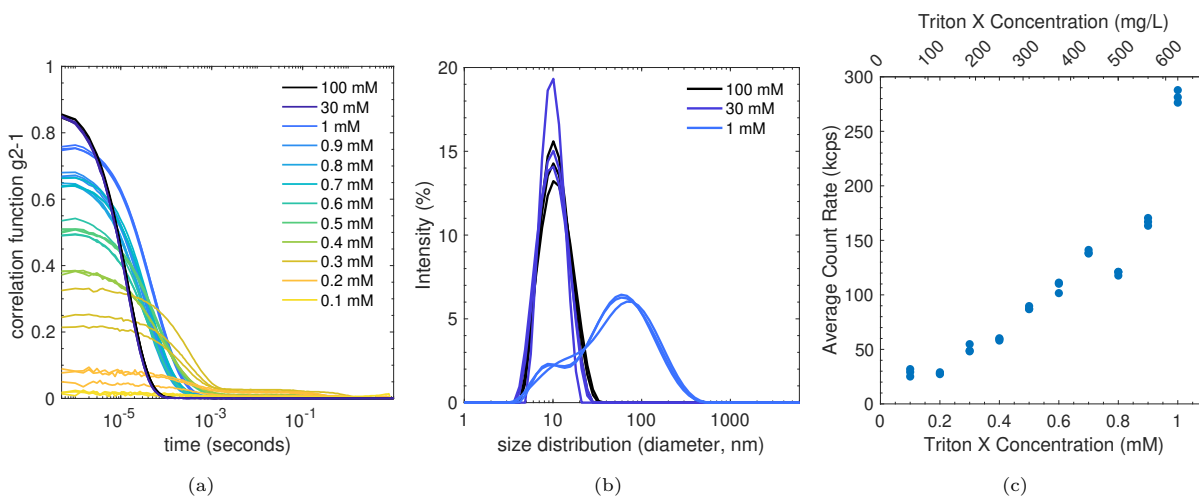


Figure 17: Dynamic light scattering results for Triton X, including a) the correlation functions for each concentration measured (color range from dark blue to yellow with decreasing concentration), b) the size distributions by percent intensity for 100, 30, and 1 mM (equivalent to 62500, 18750, 625 mg/L), and c) the average count rate (kilo counts per second) versus concentration to elucidate the CMC.

3.3.2 SDS micelle size and CMC

SDS solutions were measured on DLS with concentrations between 1 and 12 mM to elucidate the CMC, and additionally at 20, 60, and 100 mM to observe the micellar size at higher concentrations (Fig. 18). The correlation functions of the 100 and 60 mM solutions were very reproducible within each concentration, though with unexpected bumps towards the bottom of the curves, disrupting the primary exponential decay curve and indicating a secondary aggregate population (Fig. 18a). At 20 mM, the decay curve did not have a bump and was represented by a single exponential decay. Additionally, there was a noticeable

shift of the correlation functions to the right (i.e., larger time lag for the same degree of correlation) with decreasing concentration, indicating a shift to larger sizes. At concentrations lower than 12 mM, the shape of the curves became dissimilar to the higher concentrations, with more extended plateaus before the decay, which may indicate that a primary aggregate population of larger sizes was present. These lower concentrations' curves were also, however, less reproducible and less smooth, indicating lower data quality likely from a lower signal of micelles. Calculating the average hydrodynamic diameter from the correlation functions for the 100, 60, and 20 mM gave the following diameters, respectively: 4.68 ± 0.09 nm, 6.73 ± 0.31 nm, and 12.95 ± 0.24 nm. These values indeed show increasing micelle size with decreasing concentration. These values agree with, for example, Chodankar et al. (2007), who reported an average micelle diameter of 4.2 nm for a 1 wt% SDS solution (equivalent to 100 mM), measured using DLS. However, the bumps in the correlation functions indicate high polydispersity, meaning that there is more uncertainty to the calculated average hydrodynamic diameter because the calculation assumes monodisperse distributions.

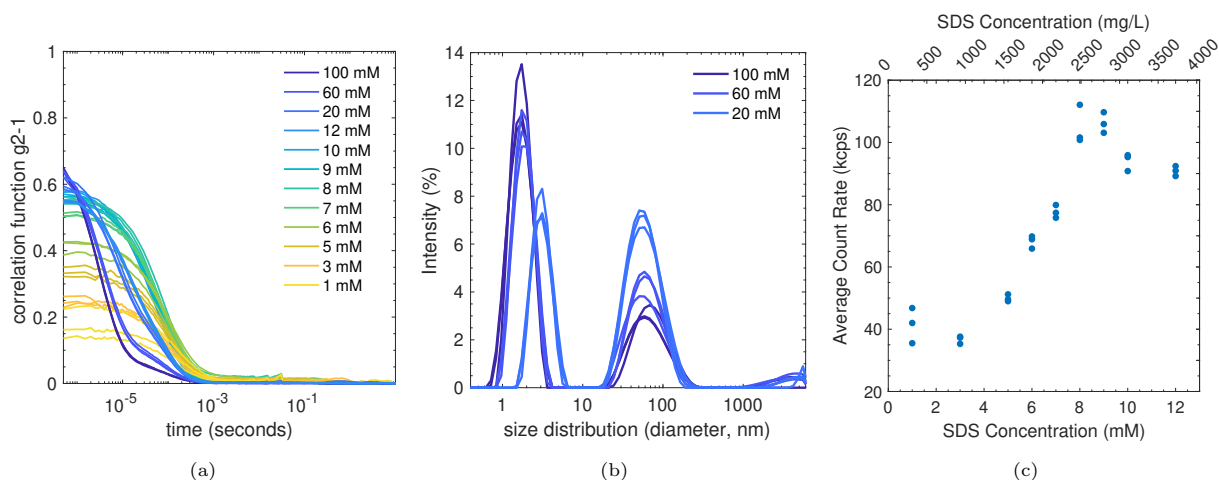


Figure 18: Dynamic light scattering results for SDS, including a) the correlation functions for each concentration measured (color range from dark blue to yellow with decreasing concentration), b) the size distributions by percent intensity for 100, 60, and 20 mM (equivalent to 28800, 17300, 5800 mg/L), and c) the average count rate (kilo counts per second) versus concentration to elucidate the CMC.

This polydispersity in the higher concentrations likely reflects the presence of larger aggregates. The possible presence of aggregates was also seen in the intensity size distribution in Figure 18b – the size distributions at both 100 and 60 mM showed primary peaks at 1.7 nm and secondary peaks at around 60 nm. At 20 mM, there were two peaks: a primary peak at 3 nm and a secondary peak at 60 nm. The bimodal size distributions indicate primary and secondary aggregation, and the high reproducibility of the curves suggests that this result was real and not due to noise. However, the volume and number size distributions (Appendix Fig. A8) of SDS showed only one peak below 10 nm for every concentration, suggesting that the presence of aggregates was small relative to the presence of primary micelles.

At concentrations below 20 mM, the size distributions were highly variable between measurements, indicating significant noise, as the correlation functions also suggested, and therefore should not be further interpreted (Appendix Fig. A8).

Finally, the average count rate plotted against the SDS concentration allowed for CMC determination (Fig. 18c). At 1 and 3 mM the average count rate was at around 25 kcps, and starting at 5 mM the count rate increased linearly until 8 mM. The count rates at 9, 10, and 12 mM did not fit with the linearity, likely due to changes the micelles' size with higher concentrations or to larger aggregate

formation. Nonetheless, these data indicate a CMC of SDS of between 3 and 5 mM. This measured CMC is lower than the expected range of 6 to 8.8 mM (Table 2), and the reason for this difference is not yet known.

3.3.3 Deoxycholate micelle size

DLS measurements on deoxycholate were performed for 100 mM and 8 mM (Fig. 19). At 100 mM, the correlation functions were highly reproducible and showed a steep decay (Fig. 19a). The calculated hydrodynamic diameter at 100 mM is 2.10 ± 0.06 nm, agreeing with a literature value of 2.5 nm for a 100 mM deoxycholate solution (Esposito et al., 1987). The intensity size distribution at 100 mM indicates the presence of secondary aggregates with a small peak at 200 nm, in addition to primary aggregates (micelles) with a peak at 1.5 nm (Fig. 19b). The volume and number size distributions (Appendix Fig. A9) however only indicate the presence of significantly smaller sizes, with a peak below 1 nm. These small diameters were at the lower limit of detection by the Malvern Zetasizer DLS, and thus should remain qualitative.

At 8 mM, however, the correlation functions were nonsensical and irreproducible, indicating an extremely low signal (Fig. 19a). A hydrodynamic diameter could thus not be calculated. The intensity size distributions additionally showed highly variable and noisy curves (Fig. 19b). This low signal indicates a lack of micelles in the 8 mM solution, even though deoxycholate had a CMC measured by pyrene fluorescence of 7.2 mM (Table 2).

A larger set of concentrations were not measured because of the low signal at 8 mM, and because of the sizes at the detection limit for 100 mM. I was thus not able to measure a CMC for deoxycholate with DLS, though it is clear from the 100 mM measurement that micelles were present at that concentration.

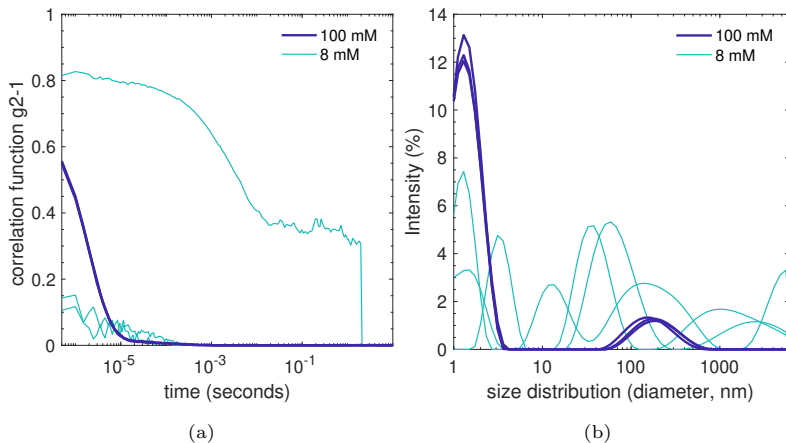


Figure 19: Dynamic light scattering results for deoxycholate, including a) the correlation functions for both concentrations measured (purple for 100 mM and blue for 8 mM), and b) the size distributions by percent intensity for 100 and 8 mM (equivalent to 41500 and 3300 mg/L).

3.3.4 Lignin aggregation sizes

Lignin solutions at 2000, 400, 200, 100, and 40 mg/L were measured with DLS (Fig. 20). The correlation functions for all concentrations had low y-intercepts, indicating poor quality measurements. At 2000 mg/L however, the curves were smooth and somewhat reproducible, which means the measurements at 2000 mg/L meet the good data quality requirements (Fig. 20a). At 400, 200, and 100 mg/L, the correlation functions were not smooth and more highly variable, further indicating poor quality DLS

measurements (Fig. 20a). Additionally, the 40 mg/L solution was so low in signal with count rates below 20 kcps that the measurement was automatically stopped early by the software and no correlation functions were produced (hence the absence of 40 mg/L in Fig. 20a,b). The poorer data quality for all the lignin measurements compared to the previously discussed compounds may be due to lignin’s higher polydispersity. Indeed, the intensity size distributions indicate multimodal, and thus polydisperse solutions (Fig. 20b). At 2000 mg/L, there was a primary peak at around 100 nm and a secondary peak at diameters around 5 nm (Fig. 20b). There was high variability, however, between the measurements. At the 400, 200, and 100 mg/L concentrations, the intensity size distribution primary peaks were also around 100 nm, similar to 2000 mg/L, but the secondary peaks were shifted to slightly larger diameters up to 11 nm. This shift indicates that aggregates are larger at smaller concentrations – a trend that was also observed for Triton X and SDS. At these lower concentrations, however, there was significant variability between measurements. Additionally, the volume and number size distributions did not show the presence of secondary aggregates (Appendix Fig. A10), indicating a small quantity of secondary aggregates relative to primary aggregates. However, volume and number size distributions of lignin should be interpreted with great caution because of the assumption of spherical particles, and it is known that lignin does not form spherical aggregates (Devarajan et al., 2020). Therefore, because DLS is best suited to monodisperse solutions of spherical particles, it may be that lignin is not accurately characterized by this technique.

The attempted CMC determination of lignin using the average count rate versus lignin concentration did not show any change in slope (Fig. 20c). The data is fairly linear with increasing average count rate with concentration, starting from the lowest concentration measured. This result indicates, like the results from the pyrene fluorescence and conductivity measurements, that there is likely no micelle formation occurring in lignin solutions. Though there may be aggregations of lignin, as evidenced by the size distributions, these aggregates do not have the same properties of micelles and micelle formation.

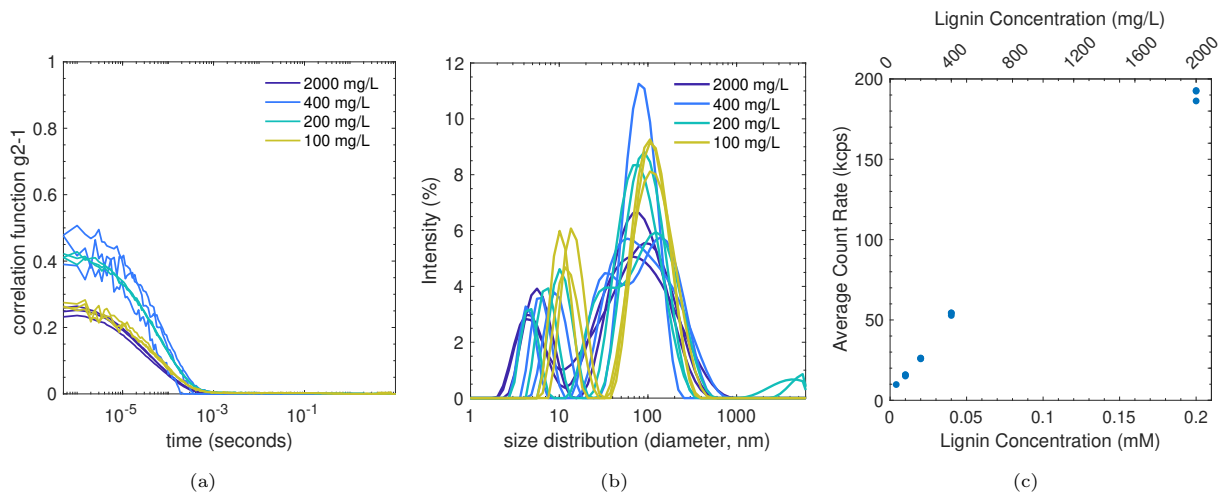


Figure 20: Dynamic light scattering results for lignin, including a) the correlation functions for four concentrations measured (purple to yellow with decreasing concentration), b) the size distributions by percent intensity for four concentrations 2000, 400, 200, and 100 mg/L (equivalent to 0.2, 0.04, 0.02, and 0.01 mM), and c) the average count rate (kilo counts per second) versus concentration to elucidate the CMC.

3.4 Ice nucleation

3.4.1 Trends in freezing temperatures

Each of the four compounds of interest were measured on our Freezing Ice Nuclei Counter (FINC) to elucidate the ice nucleation behavior with changes in concentration and micellar formation. The frozen fractions are represented as boxplots for the measured concentration series of SDS (Fig. 21a), deoxycholate (Fig. 21b), Triton X (Fig. 21c), and lignin (Fig. 21d). Boxplots can be read as follows: the middle median line is the T_{50} , where 50% of wells are frozen; the upper and lower bounds of the box are the 25th and 75th percentile, where 25 and 75% of wells are frozen; the whiskers extend to the 90th and 10th percentiles, and the outliers represent the first and last 10% of wells to freeze. Each boxplot represents one freezing experiment of 288 wells. The amount of volume used was chosen based on how active the samples were. Therefore, it is important to note that the volume of solution in the wells was not the same for each compound – for SDS and lignin, experiments used 5 μL well volume and for Triton X and deoxycholate, 10 μL well volume was used. For Triton X and deoxycholate, initial experiments using 5 μL resulted in incomplete freezing, i.e., there were still unfrozen wells remaining at $-32\text{ }^\circ\text{C}$. In order to obtain a complete frozen fraction, all the wells must freeze by the end of the experiment, and increasing the well volume to 10 μL achieved this requirement. The difference in volumes across the compounds, however, means that one cannot directly compare freezing temperatures between compounds from the boxplots, and instead one must normalize first before comparing the ice nucleating ability of the surfactants.

SDS First, the results of SDS show that at low concentrations of 0.5 and 1 mM, the freezing activity was the same as the control with a T_{50} of $-25.6\text{ }^\circ\text{C}$. At 5 mM, freezing occurred slightly warmer than the background, though it was still within the $1\text{ }^\circ\text{C}$ instrument uncertainty. At the higher concentrations of 10, 20, and 50 mM, however, the freezing temperatures were significantly warmer than the background control, with T_{50} s at -20.8 , -21.2 , and $-20.5\text{ }^\circ\text{C}$, respectively (Figure 22a). This result is intriguing, as the increase in ice nucleating activity occurred near the CMC range of SDS (between 3 and 8 mM according to my results of the CMC at $25\text{ }^\circ\text{C}$ (see Table 3) or up to 9.5 mM including the temperature dependence to $0\text{ }^\circ\text{C}$ (see Fig. 16a). This result is the first evidence of micelle formation possibly having an impact on ice nucleation.

It is still puzzling however, that with an increase in concentration above the CMC, there was no further increase in freezing temperature. One possible explanation for this result is the phase change that happens with high concentrations of SDS at sub-zero temperatures; the 20 and 50 mM samples underwent visible precipitation at around $-5\text{ }^\circ\text{C}$. In fact, a 100 mM solution was tested but precipitated and consequently the freezing could no longer be detected visually or by the freezing analysis software of FINC. This fact could mean that if there is no further increase in freezing temperature from 10 to 50 mM, the species responsible for the ice nucleation is in the supernatant rather than in the precipitate. In other words, the precipitate increases with increasing concentration while the supernatant remains the same, yet no change in freezing temperature was observed. There are thus complicating factors for interpreting the ice nucleating behavior of SDS, but it does remain clear that there was an increase in activity from below to above the CMC.

Deoxycholate A similar trend of increased freezing temperatures above the CMC was also identified for the freezing behavior of deoxycholate solutions (Fig. 21b and Fig. 22b). At the low concentrations of 0.5, 2, and 4 mM, which are below the measured CMC of 4 - 7 mM (see Table 2), the ice nucleating activity was equivalent to the background with a T_{50} of $-24.8\text{ }^\circ\text{C}$ (all within $0.5\text{ }^\circ\text{C}$ of the background).

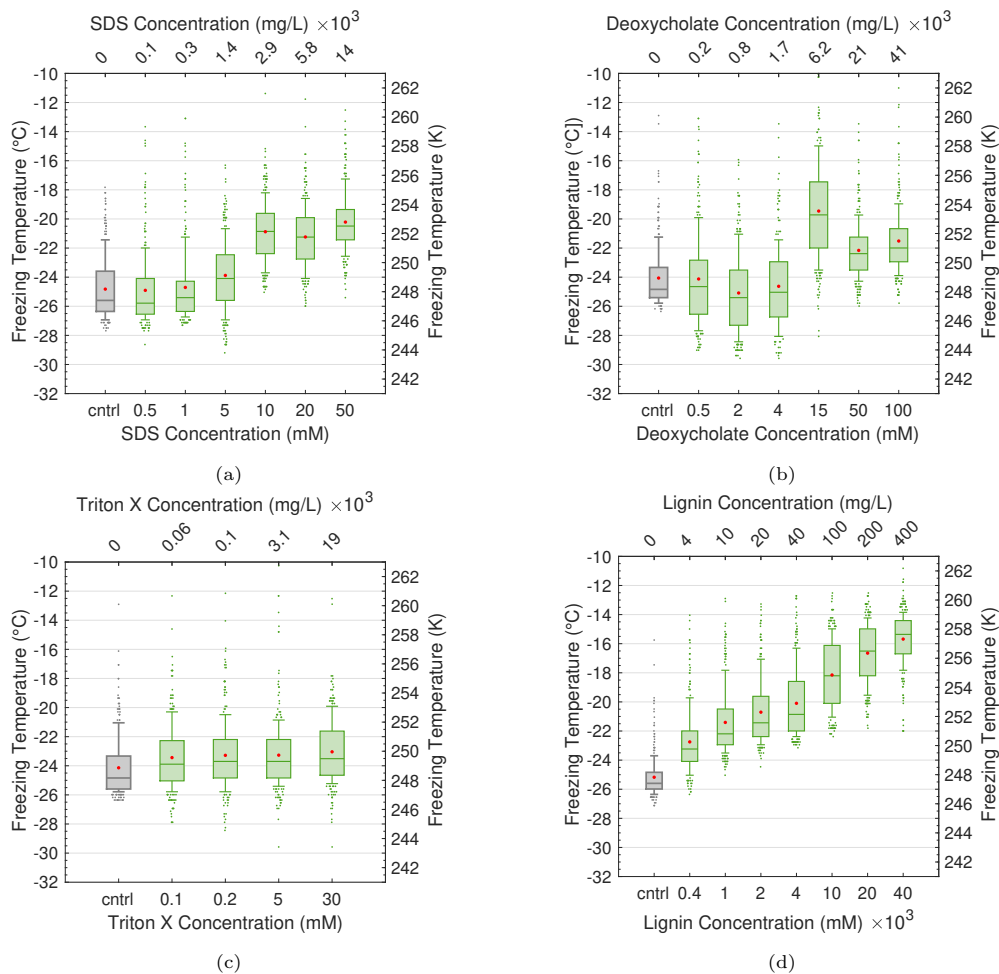


Figure 21: Frozen fractions of the concentration series of a) SDS, b) deoxycholate, c) Triton X, and d) lignin. Frozen fractions are represented with boxplots: the middle median line is the T_{50} , where 50% of wells are frozen, the upper and lower bounds of the box are the 25th and 75th percentile (where 25 and 75% of wells are frozen), the whiskers go to the 90th and 10th percentiles, and the outliers represent the first and last 10% of wells to freeze. The y-axis is the temperature corresponding to the freezing events (left in °C and right in Kelvin). The x-axis is categorical, indicating the concentration of the solution (lower axis in mM and upper axis in mg/L). Grey-colored boxplots in each subplot are the frozen fraction for the respective control experiment, consisting of filtered Sigma Aldrich background water at the appropriate volume. SDS (a) and Lignin (d) experiments used 5 μ L well volume and deoxycholate (b) and Triton X (c) used 10 μ L well volume.

For the higher concentrations of 15, 50, and 100 mM, above the CMC, the ice nucleating activity was higher than the background with T_{50} values at -19.8, -22.4, and -22 °C, respectively. It is unclear why the freezing of 15 mM was so much warmer than the others (T_{50} of 15 mM was 3 °C warmer than that of 50 mM), and why the 50 and 100 mM samples were so similar. Unlike the higher concentrations of SDS, there was no visible precipitation happening in the deoxycholate solutions. Nonetheless, similar to SDS, it is clear that the deoxycholate samples with concentration higher than the CMC froze warmer than those below the CMC.

Triton X The ice nucleating activity of Triton X did not show any trend with increasing concentration (Fig. 21c and Fig. 22c). In fact, the freezing behavior of 0.1, 0.2, 5, and 30 mM were all within 1 degree of the background control. This result means either that Triton X solutions do not induce heterogeneous ice nucleation at any concentration, or, more likely, that FINC is not sensitive enough to be able to see the ice nucleating behavior of Triton X. One would need an ice nucleation instrument that has a colder

background in order to properly elucidate the ice nucleation behavior of Triton X. An instrument which uses microfluidically generated droplets of nanoliter size, such as the devices by Stan et al. (2009), Reicher et al. (2018), Tarn et al. (2018) or Riechers et al. (2013), may be more suitable since the background freezing temperatures are around -35 °C. Because of the warmer background of FINC, I cannot conclude whether there is a difference in ice nucleating activity with the presence of micelles in Triton X.

Lignin The freezing boxplots of the lignin concentration series show warmer freezing temperatures with increasing lignin concentration (Fig. 21d). Notably, the trend is nonlinear – the plot of T_{50} versus concentration illuminates a logarithmically increasing T_{50} with concentration. This trend is very similar to what was reported recently in Bogler and Borduas-Dedekind (2020), though the T_{50} values were higher here. The T_{50} appears to approach an asymptote, where at a certain concentration, a further increase in concentration does not result in warmer freezing. This trend is surprisingly similar to the freezing behavior observed for SDS and deoxycholate, where at a specific concentration there was no further increase in freezing temperature. This result indicates that there is likely an effect of supramolecular structure of ice nucleation, analogous to SDS and deoxycholate. The effect of concentration can further be elucidated when the freezing data is converted into INP active sites per milligram of each compound, as described in the following section.

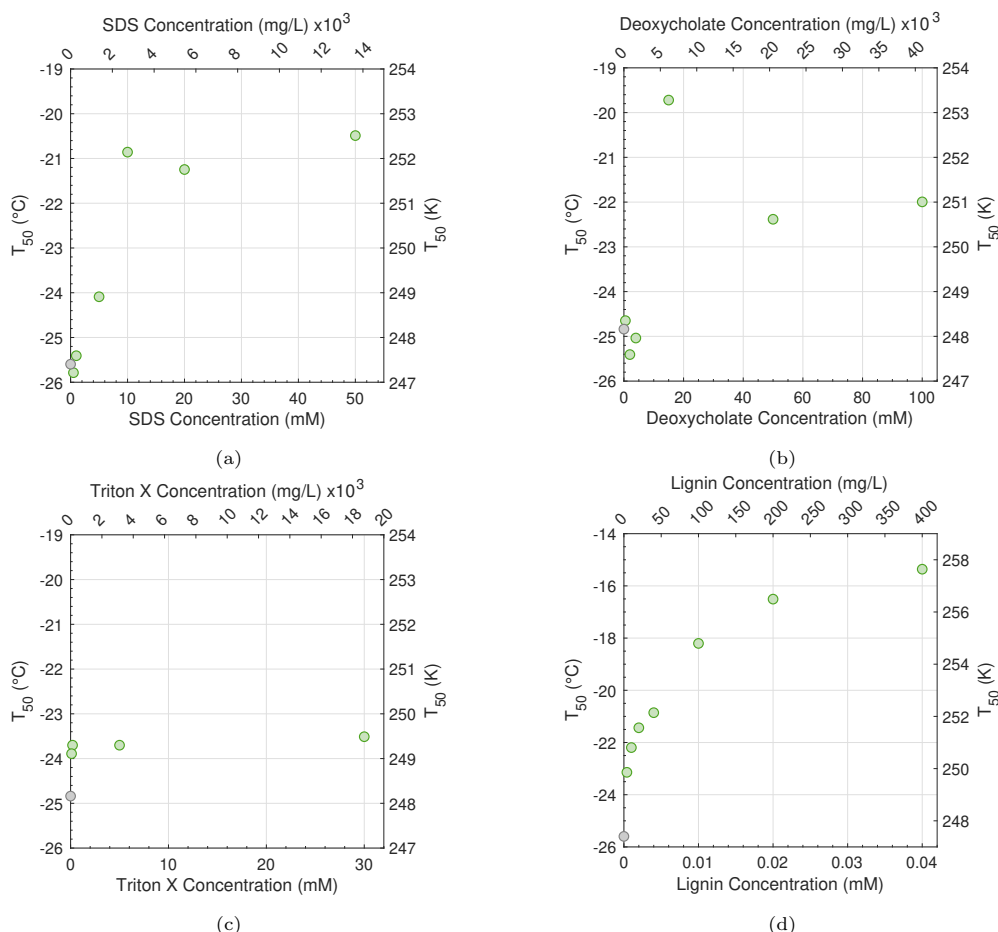


Figure 22: T_{50} values (the temperature at which 50% of the wells are frozen) versus concentration for a) SDS, b) deoxycholate, c) Triton X, and d) lignin. SDS (a) and lignin (d) experiments used $5 \mu\text{L}$ well volume and deoxycholate (b) and Triton X (c) used $10 \mu\text{L}$ well volume. Y-axes are temperature (left °C and right Kelvin) and x-axes are concentration (bottom mM, top mg/L).

3.4.2 Ice nucleating activity normalized to carbon concentration

To compare ice nucleating activity across the four compounds measured and to compare across the different concentrations, I converted the frozen fraction data to the ice-active mass site density, n_m . The ice-active mass site density is defined as the number of sites causing nucleation per unit mass of the ice nucleating particle or macromolecule (Kanji et al., 2017; Vali, 2019) and is calculated by:

$$n_m[\text{mgC}^{-1}] = -\frac{\ln[1 - \text{FF}(T)]}{\text{TOC} * V_{\text{well}}} \quad (5)$$

where $\text{FF}(T)$ is the frozen fraction at each temperature, TOC is the total concentration of organic carbon in the sample (in mg/L) and V_{well} is the volume of the solution in each well (in L). n_m is thus a function of temperature. I use the concentration of organic carbon, rather than the molarity or the total mass, to better compare to the literature (e.g T. W. Wilson et al., 2015; Borduas-Dedekind et al., 2019; Bogler & Borduas-Dedekind, 2020; Miller et al., 2020). TOCs were calculated for SDS, deoxycholate, and Triton X using the molar ratio of carbon in the molecules, and for lignin the manufacturer value of lignin being 50% carbon by mass was used. Finally, it is important to note that n_m curves are only calculated for frozen fractions significantly different from the background control, therefore excluding all Triton X freezing data. This limit exists because the active site theory depends on there being heterogeneous ice nucleation by the added compounds, and if the freezing is the same as the clean water background, one cannot say that ice nucleation was due to the added compound.

SDS In SDS n_m plots, the two highest concentrations of 50 and 20 mM have nearly identical n_m curves, ranging from 0.01 sites/mgC at -13 °C to 400 sites/mgC at -26 °C (Fig. 23a). The lowest concentration of 5 mM overlays these two but extends to 1000 sites/mgC at -29 °C (Fig. 23a). The result of the 50, 20, and 5 mM n_m curves overlaying each other indicates that the differences in their freezing temperatures (Fig. 21a) were due to their differences in concentration. The 10 mM curve however is shifted up to higher n_m s for each temperature, with n_m s ranging from 0.4 sites/mgC at -15 °C to 900 sites/mgC at -25 °C/ (Fig. 23a). Because the 10 mM n_m curve does not overlay the others, it reveals that their difference in freezing temperatures was not due to the change in concentration. However, the difference is small and may be within the variability of the instrument. Indeed, in freezing tests of a second concentration series of SDS, the 10 mM and 5 mM n_m curves were overlapping (Appendix Fig. A11). Overall, the n_m plots of SDS indicate that for solutions freezing above the background, the ice nucleating activity seems to scale with concentration. Since the concentrations are above the CMC, micelles are present and are also increasing in number with increasing concentration. Thus, the ice nucleating activity appears to also scale with micelle concentration according to the n_m calculations.

Note that when comparing n_m values of SDS to previously reported n_m parameterizations of sea-surface water (T. W. Wilson et al., 2015) and lignin (Miller et al., 2020), SDS had lower n_m s at -20 °C by two orders of magnitude from lignin and four orders of magnitude from sea-surface water (Fig. 23a). This result indicates that SDS was less ice-active per mg carbon than ice nucleating particles in the sea surface and in lignin solutions.

Deoxycholate The n_m plots for deoxycholate show overlapping curves of the 100 mM and 50 mM concentrations, with n_m s extending from 0.04 sites/mgC at -12 °C to 110 site/mgC at -26 °C (Fig. 23b). The 15 mM n_m curve however is significantly shifted up to higher n_m s and is less steep than the others, with n_m s ranging from 0.3 sites/mgC at -8 °C to 500 sites/mgC at -25 °C (Fig. 23b). The overlapping nature of the 100 and 50 mM curves reveal that differences in their freezing temperatures were due to

differences in concentration, as seen for SDS. The 15 mM curve however appears to be an outlier because the curve is so far from the others. It was also clear from the boxplots that the 15 mM was an outlier, thus suggesting perhaps contamination in that sample. Further tests to replicate these results would be needed to assess true differences.

Further, similarly to SDS, deoxycholate was less ice-active than samples from sea-surface water (T. W. Wilson et al., 2015) and of lignin (Miller et al., 2020), as shown by the comparison in Fig. 23b. The deoxycholate concentrations of 100 and 50 mM were four orders of magnitude less active than lignin and six orders of magnitude less active than the sea-surface water samples at -20 °C.

Lignin The n_m plot presented here for lignin shows overlapping curves for every concentration measured on FINC (Fig. 23c). However, there is a noticeable trend of increasing n_m s with increasing concentration: at 400 mg/L, the n_m s extend from 3 sites/mgC at -11 °C to 5,000 sites/mgC at -23 °C, whereas at 4 mg/L lignin the n_m s range from 300 sites/mgC at -14 °C to 600,000 sites/mgC at -27 °C (Fig. 23c). This trend of increasing sites with increasing concentration is in fact reported by Bogler and Borduas-Dedekind (2020), though they showed a much starker trend with greater differences between concentrations. The inconsistencies between my results and those reported by Bogler and Borduas-Dedekind (2020) are hypothesized to be due to differences in the product batch of lignin used or differences in the well-volume, and how lignin molecules interact with the wells at different volumes and concentrations. Finally, note that the lignin n_m values here also match well with the parameterization of lignin from Miller et al. (2020) (Fig. 23c), though values here are up to half an order of magnitude higher (at -17 °C). Again, these differences may be due to variations in batches or well volume. These differences between the lignin ice nucleating activity reported here, in Bogler and Borduas-Dedekind (2020), and in Miller et al. (2020) are still being investigated.

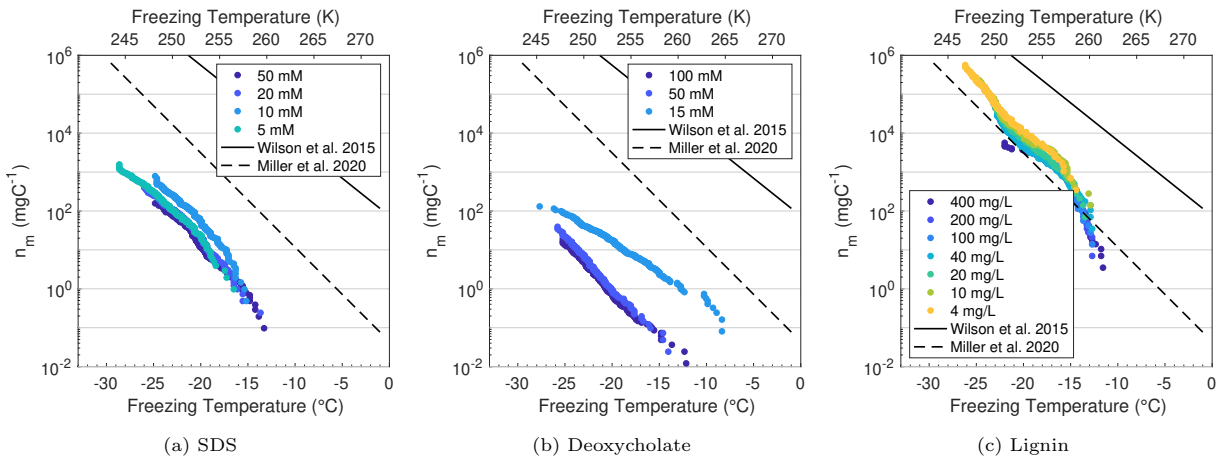


Figure 23: Ice-active mass site densities n_m versus temperature for a concentration series of a) SDS (50, 20, 10, 5 mM), b) deoxycholate (100, 50, 15 mM), and c) Lignin (400, 200, 100, 40, 20, 10, 4 mg/L). n_m s were calculated using TOC values for SDS, deoxycholate, and Triton X based on number of carbon atoms in their molecular structures, and TOC for lignin was taken as 50% of total mass as reported by the manufacturing details. For reference, two parameterizations are shown: T. W. Wilson et al. (2015) n_m of sea-spray aerosol (solid black line), and Miller et al. (2020) n_m of lignin (dashed black line).

4 Discussion

In all, the micelle probing experiments allowed us to measure the CMC of SDS, sodium deoxycholate, and Triton X-100 using pyrene fluorescence, conductivity, and DLS (Table 3). The CMC of SDS (7.6 - 8.5 mM) could be elucidated with these methods, although DLS measurements appeared to underestimate the CMC range. The CMC of deoxycholate could only be measured using pyrene fluorescence (7.2 ± 0.3 mM), due to limitations with the size of particles able to be measured by the DLS technique and due to an unknown issue with the conductivity measurements. Triton X’s CMC was measured with pyrene fluorescence and DLS and had a range of 0.2 - 0.44 mM. Since Triton X is nonionic, the conductivity method was not used. In addition, DLS proved useful for measuring the size distributions of the aggregates in solution for all compounds (Table 3). These results highlight the importance of using several different methods to obtain enough data on these three micelle-forming surfactants.

Unlike the other compounds, a CMC of lignin could not be measured using these micelle-probing methods, confirming the absence of micelles in lignin solutions (Table 3). It may be that there is aggregation but without formation of micelles. The DLS measurements indeed provide preliminary evidence for the presence of aggregates in lignin solutions, as the size distributions show particle diameters both under 10 nm and over 100 nm. Additionally, Devarajan et al. (2020) recently published evidence that lignin molecules associate with each other to form larger aggregations, as modelled by molecular dynamics simulations. It is likely that because lignin is composed of complex and diverse molecules, regularly shaped and sized aggregate structures are unlikely to form, thus making it more challenging to characterize the structure (Devarajan et al., 2020).

Connecting the supramolecular structure of the studied compounds to their freezing behavior resulted in discovering that the ice nucleating activity of SDS and deoxycholate increased above the CMC (Table 3; Fig. 21, 22). Unfortunately, Triton X was not ice active in immersion freezing above the detection limit of our FINC instrument. For lignin, since there was no CMC, a correlation between ice nucleation and micelle formation cannot be made. Nonetheless, I can affirm the observation of an asymptotic trend of freezing temperatures with increasing concentration consistent with Bogler and Borduas-Dedekind (2020), as was also observed in the micelle-forming surfactants (Fig. 22d, 22a, 22b).

Table 3: Summary of results of micelle probing and ice nucleation activity (INA) trends for each compound. Pyrene 1:3 method was performed at 29 °C; conductivity and DLS measurements reported here were taken at 25 °C. Pyrene 1:3 CMCs reported use the $CMC_{method1}$ for Triton X and $CMC_{method2}$ for SDS and deoxycholate, as recommended by Aguiar et al. (2003). DLS diameters reported are using the average hydrodynamic diameter at 100 mM for SDS, Triton X, and deoxycholate, and for lignin the diameters reported are the ranges of the peak of the intensity size distributions for all concentrations measured.

Compound	Pyrene 1:3 CMC (mM)	Conductivity CMC (mM)	DLS CMC (mM)	DLS diameter (nm)	INA change with micelles?
SDS	8.0 ± 0.5	7.60 – 7.95	3 – 5	4.68 ± 0.09	Increase
Deoxycholate	7.2 ± 0.3	None	n/a	2.10 ± 0.06	Increase
Triton X	0.38 ± 0.06	Nonconductive	0.2 – 0.3	10.0 ± 0.1	At LOD
Lignin	None	None	None	2 – 15 / 60 – 200	No CMC

An outstanding question is why do the different micelle-forming surfactants have different ice nucleating abilities? For example, why is Triton X not as ice-active as SDS and deoxycholate, despite all three substances having the ability to make micelles? A possible hypothesis is that it is because Triton X uniquely has unimodal size distributions observed in the DLS measurements of 100 and 30 mM, where the single size peak is at 10 nm (Fig. 17). SDS and deoxycholate, on the other hand, have multimodal size distributions showing the presence of aggregates larger than 100 nm in diameter for the concentrations measured on FINC (Fig. 18 and 19). The fact that there were no aggregates larger than 100 nm measured by DLS in the most concentrated Triton X solutions, and that Triton X also did not show ice nucleating activity above the background, may indicate that secondary aggregates (i.e., aggregates of micelles) are required for surfactants to nucleate ice. This correlation leads to a second hypothesis that a size requirement of approximately 100 nm is needed for a substance to be ice nucleating. The DLS and FINC results of lignin additionally support this idea, as lignin solutions contained primarily sizes at or larger than 100 nm (Fig. 3.3.4) and had high ice nucleating activity (Fig. 23c). A third possible hypothesis as to why Triton X is not ice nucleating is that Triton X is nonionic, and SDS, deoxycholate, and lignin are ionic. Ionic interactions of the molecules with themselves and with water may help order water molecules and induce ice nucleation (e.g., Glatz & Sarupria, 2016). To strengthen these theories, testing a more extensive set of micelle-forming surfactants would be beneficial.

The findings in this thesis contribute well to the literature. For a long time, the accepted size range of ice-active particles extended to no smaller than 100 nm (P. K. Wang, 2013). The results here suggesting that larger aggregates of at least 100 nm nucleate ice thus corroborate the traditional size range. However, more recent literature suggests ice nucleation by considerably smaller moieties. For example, Pummer et al. (2015), O’Sullivan et al. (2015), and Eickhoff et al. (2019), report ice nucleation by macromolecules as small as 4 nm at -25 °C and 8 nm at -10 °C, as measured by size filtration experiments. Therefore, my results deviate from these studies because I found that Triton X micelles of 10 nm diameter did not nucleate ice warmer than -25 °C, and SDS, deoxycholate, and lignin containing larger aggregates did nucleate warmer than -25 °C. It is also possible, however, that in these previous papers, aggregates of the sub-10 nm macromolecules were causing ice nucleation and not the individual macromolecules – their research did not address this possibility. Indeed, there have been few studies explicitly investigating the role of aggregates of smaller macromolecules on ice nucleation, as I did here. Cascajo-Castresana et al. (2020) was one such study that used DLS measurements to positively correlate ice activity of a protein to the presence of aggregates, rather than the protein monomers. The results of this thesis complement Cascajo-Castresana et al. (2020), and our studies together suggest the use of dynamic light scattering as a valuable method worth pursuing for characterizing ice-active substances.

5 Atmospheric Implications

This thesis explored the role of aggregation and supramolecular structure on the ice nucleation of droplets through the analysis of three micelle-forming surfactants (sodium dodecyl sulfate (SDS), sodium deoxycholate, and Triton X-100) and the organic plant polymer lignin. I found that for ice nucleation to occur above the background in our freezing instrument FINC, it may be necessary for secondary aggregates larger than 100 nm to be present.

When extrapolating the relevance of this thesis to the atmosphere, the concentration of surfactants in aerosol must be discussed. Gérard et al. (2019) reported concentrations of amphiphilic surfactants in collected atmospheric aerosol from three locations (representing coastal, remote inland, and urban

areas) on multiple sampling days. They found that for the urban (53 samples) and remote (142 samples) locations, surfactants were present in at least 100 mM concentrations for 18 urban and 37 remote sampling days. They additionally found concentrations above 900 mM for two days at each site. Further, Gérard et al. (2019) measured the CMCs for each sample and found a range of 0.01 to 1 mM. These results clearly suggest that surfactants are present in real atmospheric aerosol samples at concentrations up to 100,000 times higher than the critical micelle concentration, thus high enough concentrations to form micelles *and* secondary aggregates of micelles. However, note that the concentration of surfactants would decrease if these surfactant-containing aerosol become diluted when growing into cloud droplets. Still, if surfactants can be present in concentrations as high as 1000 mM and have CMCs as low as 0.01 mM, then several orders of magnitude of dilution would still result in a concentration high enough for micelles and secondary aggregates to form. Thus, it is possible that surfactants in aerosol may initiate ice nucleation in clouds.

A second significant consideration for atmospheric relevance is that of atmospheric aerosol chemical composition. In the experiments conducted in this thesis, only single-compound solutions were measured. In reality, atmospheric aerosol and cloud droplets are composed of diverse compounds in various concentrations, including but not limited to mineral dusts, complex organic matter, and salts (Seinfeld & Pandis, 2006). Salts, such as NaCl, are known to decrease the CMC (Corrin & Harkins, 1947; Rosen & Kunjappu, 2012). Therefore, surfactants' CMCs in real atmospheric aerosol are likely smaller than those measured here due to the salt content in aerosol, and thus micelles and aggregates would form at lower concentrations. Further, Devarajan et al. (2020) recently showed with molecular dynamics simulations that the aggregations of dissolved organic matter (DOM) depend not only on salt ion concentration, but on the type of ion. Specifically, a calcium cation was more effective at bridging molecules to form aggregates than other cations. Devarajan et al. (2020) also illustrated the complexity of aggregation behavior of DOM, including that aggregation changes depend on which components are present. Similarly, micelle-forming surfactants are affected by the presence of additives, such as other micelle-forming surfactants or different types of organic molecules (Rosen & Kunjappu, 2012). Therefore, to assess the effects of aggregation on ice nucleation in real atmospheric droplets, it is imperative to also conduct micelle-probing and freezing experiments with mixed systems, containing various mixtures of micelle-forming surfactants, complex organic matter, and salts.

6 Outlook

The effect of surfactants and aggregation on atmospheric ice nucleation was explored in this thesis. To further the findings of this work, characterizing the freezing behavior of a larger set of micelle-forming surfactants, as well as mixed systems, with the methods employed here would be highly useful. Other methods to complement the research could include using an optical drop-shape tensiometer to measure the surface tensions of the surfactant solutions (e.g., Berry et al., 2015; Gérard et al., 2019; Bzdek et al., 2020). A drop-shape tensiometer with a temperature control unit (e.g., the OCA series from DataPhysics) would have the added advantage of measuring the surfactant behavior at sub-zero temperatures because of the microliter sized droplets used. These measurements would provide a unique insight into the temperature dependence of micelle formation in supercooled droplets, which is highly relevant to real atmospheric aerosol.

7 Acknowledgements

First and foremost, I would like to thank Dr. Nadine Borduas-Dedekind for being an excellent supervisor and mentor. Your unwavering support – academically and personally – was a huge help to me throughout this process, and I truly appreciate your dedication to me and my project. We were both new to the topic of surfactants, and it was a lot of fun to dive into this together. I also want to thank Dr. Claudia Marcolli for being my second reader and providing valuable feedback on the project. Pointing us toward the dynamic light scattering technique indeed proved very useful.

My appreciation further goes to Mattia Cerri for suggesting the pyrene fluorescence technique and guiding me through the experimental procedure. Particular thanks also to Mattia Usuelli and the group of Prof. Dr. Raffaele Mezzenga in Food Sciences for giving me access to the Malvern Zetasizer for DLS measurements. Mattia took a lot of his time to teach me about DLS and to guide me through the measurements and data analysis, and I am very grateful for that.

I want to extend my gratitude also to the NBD group. It has been such a pleasure being a part of this team. My thanks especially go to Sophie Bogler for the many lignin discussions, for feedback on my writing, and for just being a good friend. Thank you also to Jon Went for help with FINC measurements. More special thanks go to Sebastian Zala for being a great office buddy, making work much more enjoyable.

Further acknowledgments go to the McNeill and Lohmann groups. I always appreciated the discussions with group members, and I am glad to have had the support of so many. Special shout-out to fellow group member and close friend Ulrike Proske for asking tough questions and always being someone I could talk to, thesis-related or otherwise.

Finally, thank you to my family. The weekly Zooms with my parents Celeste and Dan and my sister Georgia have been a continued source of support and motivation. Calls also with my long-distance best friends were crucial for keeping me sane. Last but not least, endless thanks to my partner Johanna for her daily love, support, and encouragement.

8 References

- Abdelmonem, A., Backus, E. H. G., Hoffmann, N., Sánchez, M. A., Cyran, J. D., Kiselev, A., & Bonn, M. (2017). Surface-charge-induced orientation of interfacial water suppresses heterogeneous ice nucleation on alpha-alumina (0001). *Atmos. Chem. Phys.*, *17*(12), 7827–7837. <https://doi.org/10.5194/acp-17-7827-2017>
- Aguiar, J., Carpena, P., Molina-Bolivar, J. A., & Carnero Ruiz, C. (2003). On the determination of the critical micelle concentration by the pyrene 1:3 ratio method. *Journal of Colloid and Interface Science*, *258*(1), 116–122. [https://doi.org/10.1016/S0021-9797\(02\)00082-6](https://doi.org/10.1016/S0021-9797(02)00082-6)
- Asa-Awuku, A., Sullivan, A. P., Hennigan, C. J., Weber, R. J., & Nenes, A. (2008). Investigation of molar volume and surfactant characteristics of water-soluble organic compounds in biomass burning aerosol. *Atmos. Chem. Phys.*, *14*.
- Augustin, S., Wex, H., Niedermeier, D., Pummer, B., Grothe, H., Hartmann, S., Tomsche, L., Clauss, T., Voigtländer, J., Ignatius, K., & Stratmann, F. (2013). Immersion freezing of birch pollen washing water. *Atmospheric Chemistry and Physics*, *13*(21), 10989–11003. <https://doi.org/10.5194/acp-13-10989-2013>
- Baduel, C., Nozière, B., & Jaffrezo, J.-L. (2012). Summer/winter variability of the surfactants in aerosols from Grenoble, France. *Atmospheric Environment*, *47*, 413–420. <https://doi.org/10.1016/j.atmosenv.2011.10.040>
- Berne, B. J., & Pecora, R. (2000). *Dynamic Light Scattering: With Applications to Chemistry, Biology, and Physics*. Courier Corporation.
- Berry, J. D., Neeson, M. J., Dagastine, R. R., Chan, D. Y., & Tabor, R. F. (2015). Measurement of surface and interfacial tension using pendant drop tensiometry. *Journal of Colloid and Interface Science*, *454*, 226–237. <https://doi.org/10.1016/j.jcis.2015.05.012>
- Boerjan, W., Ralph, J., & Baucher, M. (2003). Lignin biosynthesis. *Annual Review of Plant Biology*, *54*(1), 519–546. <https://doi.org/10.1146/annurev.arplant.54.031902.134938>
- Bogler, S., & Borduas-Dedekind, N. (2020). Lignin’s ability to nucleate ice via immersion freezing and its stability towards physicochemical treatments and atmospheric processing. <https://doi.org/10.5194/acp-2020-589>
- Borduas-Dedekind, N., Ossola, R., David, R. O., Boynton, L. S., Weichlinger, V., Kanji, Z. A., & McNeill, K. (2019). Photomineralization mechanism changes the ability of dissolved organic matter to activate cloud droplets and to nucleate ice crystals. *Atmos. Chem. Phys.*, *19*(19), 12397–12412. <https://doi.org/10.5194/acp-19-12397-2019>
- Bzdek, B. R., Reid, J. P., Malila, J., & Prisle, N. L. (2020). The surface tension of surfactant-containing, finite volume droplets. *PNAS*, *117*(15), 8335–8343. <https://doi.org/10.1073/pnas.1915660117>
- Carpena, P., Aguiar, J., Bernaola-Galván, P., & Carnero Ruiz, C. (2002). Problems associated with the treatment of conductivity-concentration data in surfactant solutions: Simulations and experiments. *Langmuir*, *18*(16), 6054–6058. <https://doi.org/10.1021/la025770y>
- Cascajo-Castresana, M., David, R. O., Iriarte-Alonso, M. A., Bittner, A. M., & Marcolli, C. (2020). Protein aggregates nucleate ice: The example of apoferritin. *Atmos. Chem. Phys.*, *20*(6), 3291–3315. <https://doi.org/10.5194/acp-20-3291-2020>
- Chodankar, S., Aswal, V. K., Hassan, P. A., & Wagh, A. G. (2007). Structure of protein–surfactant complexes as studied by small-angle neutron scattering and dynamic light scattering. *Physica B: Condensed Matter*, *398*(1), 112–117. <https://doi.org/10.1016/j.physb.2007.05.003>

- Cieřla, J., Bieganowski, A., Narkiewicz-Michalek, J., & Szymula, M. (2013). Use of a dynamic light scattering technique for SDS/water/pentanol studies. *Journal of Dispersion Science and Technology*, *34*(4), 566–574. <https://doi.org/10.1080/01932691.2012.680834>
- Cochran, R. E., Laskina, O., Jayarathne, T., Laskin, A., Laskin, J., Lin, P., Sultana, C., Lee, C., Moore, K. A., Cappa, C. D., Bertram, T. H., Prather, K. A., Grassian, V. H., & Stone, E. A. (2016). Analysis of organic anionic surfactants in fine and coarse fractions of freshly emitted sea spray aerosol. *Environ. Sci. Technol.*, *50*(5), 2477–2486. <https://doi.org/10.1021/acs.est.5b04053>
- Corrin, M. L., & Harkins, W. D. (1947). The effect of salts on the critical concentration for the formation of micelles in colloidal electrolytes. *J. Am. Chem. Soc.*, *69*(3), 683–688. <https://doi.org/10.1021/ja01195a065>
- David, R. O., Cascajo-Castresana, M., Brennan, K. P., Rösch, M., Els, N., Werz, J., Weichlinger, V., Boynton, L. S., Bogler, S., Borduas-Dedekind, N., Marcolli, C., & Kanji, Z. A. (2019). Development of the DRoplet Ice Nuclei Counter Zurich (DRINCZ): Validation and application to field-collected snow samples. *Atmos. Meas. Tech.*, *12*(12), 6865–6888. <https://doi.org/10.5194/amt-12-6865-2019>
- DeMott, P. J., Prenni, A. J., Liu, X., Kreidenweis, S. M., Petters, M. D., Twohy, C. H., Richardson, M. S., Eidhammer, T., & Rogers, D. C. (2010). Predicting global atmospheric ice nuclei distributions and their impacts on climate. *Proceedings of the National Academy of Sciences*, *107*(25), 11217–11222. <https://doi.org/10.1073/pnas.0910818107>
- DeMott, P. J., Mason, R. H., McCluskey, C. S., Hill, T. C. J., Perkins, R. J., Desyaterik, Y., Bertram, A. K., Trueblood, J. V., Grassian, V. H., Qiu, Y., Molinero, V., Tobo, Y., Sultana, C. M., Lee, C., & Prather, K. A. (2018). Ice nucleation by particles containing long-chain fatty acids of relevance to freezing by sea spray aerosols. *Environ. Sci.: Processes Impacts*, *20*(11), 1559–1569. <https://doi.org/10.1039/C8EM00386F>
- Devarajan, D., Liang, L., Gu, B., Brooks, S. C., Parks, J. M., & Smith, J. C. (2020). Molecular dynamics simulation of the structures, dynamics, and aggregation of dissolved organic matter. *Environ. Sci. Technol.*, *54*(21), 13527–13537. <https://doi.org/10.1021/acs.est.0c01176>
- Dharaiya, N., & Bahadur, P. (2012). Phenol induced growth in Triton X-100 micelles: Effect of pH and phenols’ hydrophobicity. *Colloids and Surfaces A: Physicochemical and Engineering Aspects*, *410*, 81–90. <https://doi.org/10.1016/j.colsurfa.2012.06.021>
- Dreischmeier, K., Budke, C., Wiehemeier, L., Kottke, T., & Koop, T. (2017). Boreal pollen contain ice-nucleating as well as ice-binding ‘antifreeze’ polysaccharides. *Scientific Reports*, *7*(1). <https://doi.org/10.1038/srep41890>
- Eickhoff, L., Dreischmeier, K., Zipori, A., Sirovinskaya, V., Adar, C., Reicher, N., Braslavsky, I., Rudich, Y., & Koop, T. (2019). Contrasting behavior of antifreeze proteins: Ice growth inhibitors and ice nucleation promoters. *J. Phys. Chem. Lett.*, *10*(5), 966–972. <https://doi.org/10.1021/acs.jpcclett.8b03719>
- Esposito, G., Giglio, E., Pavel, N. V., & Zanobi, A. (1987). Size and shape of sodium deoxycholate micellar aggregates. *J. Phys. Chem.*, *91*(2), 356–362. <https://doi.org/10.1021/j100286a023>
- Forestieri, S. D., Staudt, S. M., Kuborn, T. M., Faber, K., Ruehl, C. R., Bertram, T. H., & Cappa, C. D. (2018). Establishing the impact of model surfactants on cloud condensation nuclei activity of sea spray aerosol mimics. *Atmos. Chem. Phys.*, *18*(15), 10985–11005. <https://doi.org/10.5194/acp-18-10985-2018>

- Frka, S., Dautović, J., Kozarac, Z., Čosović, B., Hoffer, A., & Kiss, G. (2012). Surface-active substances in atmospheric aerosol: An electrochemical approach. *Tellus B: Chemical and Physical Meteorology*, *64*(1), 18490. <https://doi.org/10.3402/tellusb.v64i0.18490>
- Frossard, A. A., Gérard, V., Duplessis, P., Kinsey, J. D., Lu, X., Zhu, Y., Bisgrove, J., Maben, J. R., Long, M. S., Chang, R. Y.-W., Beaupré, S. R., Kieber, D. J., Keene, W. C., Nozière, B., & Cohen, R. C. (2019). Properties of seawater surfactants associated with primary marine aerosol particles produced by bursting bubbles at a model air–sea interface. *Environ. Sci. Technol.*, *53*(16), 9407–9417. <https://doi.org/10.1021/acs.est.9b02637>
- Gérard, V., Nozière, B., Baduel, C., Fine, L., Frossard, A. A., & Cohen, R. C. (2016). Anionic, cationic, and nonionic surfactants in atmospheric aerosols from the Baltic Coast at Askö, Sweden: Implications for cloud droplet activation. *Environ. Sci. Technol.*, *50*(6), 2974–2982. <https://doi.org/10.1021/acs.est.5b05809>
- Gérard, V., Nozière, B., Fine, L., Ferronato, C., Singh, D. K., Frossard, A. A., Cohen, R. C., Asmi, E., Lihavainen, H., Kivekäs, N., Aurela, M., Brus, D., Frka, S., & Cvitešić Kušan, A. (2019). Concentrations and adsorption isotherms for amphiphilic surfactants in PM1 aerosols from different regions of Europe. *Environ. Sci. Technol.*, *53*(21), 12379–12388. <https://doi.org/10.1021/acs.est.9b03386>
- Glatz, B., & Sarupria, S. (2016). The surface charge distribution affects the ice nucleating efficiency of silver iodide. *J. Chem. Phys.*, *145*(21), 211924. <https://doi.org/10.1063/1.4966018>
- Glatz, B., & Sarupria, S. (2018). Heterogeneous ice nucleation: Interplay of surface properties and their impact on water orientations. *Langmuir*, *34*(3), 1190–1198. <https://doi.org/10.1021/acs.langmuir.7b02859>
- Govindarajan, A. G., & Lindow, S. E. (1988). Phospholipid requirement for expression of ice nuclei in *Pseudomonas syringae* and in vitro. *J. Biol. Chem.*, *263*(19), 9333–9338.
- Guetzloff, T. F., & Rice, J. A. (1994). Does humic acid form a micelle? *Science of The Total Environment*, *152*(1), 31–35. [https://doi.org/10.1016/0048-9697\(94\)90548-7](https://doi.org/10.1016/0048-9697(94)90548-7)
- Gurian-Sherman, D., & Lindow, S. E. (1993). Bacterial ice nucleation: Significance and molecular basis. *The FASEB Journal*, *7*(14), 1338–1343. <https://doi.org/10.1096/fasebj.7.14.8224607>
- Hallett, F. R. (1994). Particle size analysis by dynamic light scattering. *Food Res. Int.*, *27*, 4.
- Heymsfield, A. J., Schmitt, C., Chen, C.-C.-J., Bansemer, A., Gettelman, A., Field, P. R., & Liu, C. (2020). Contributions of the liquid and ice phases to global surface precipitation: Observations and global climate modeling. *Journal of the Atmospheric Sciences*, *77*(8), 2629–2648. <https://doi.org/10.1175/JAS-D-19-0352.1>
- Hill, T. C. J., DeMott, P. J., Tobo, Y., Fröhlich-Nowoisky, J., Moffett, B. F., Franc, G. D., & Kreidenweis, S. M. (2016). Sources of organic ice nucleating particles in soils. *Atmos. Chem. Phys.*, *16*(11), 7195–7211. <https://doi.org/10.5194/acp-16-7195-2016>
- Horiuchi, S., & Winter, G. (2015). CMC determination of nonionic surfactants in protein formulations using ultrasonic resonance technology. *European Journal of Pharmaceutics and Biopharmaceutics*, *92*, 8–14. <https://doi.org/10.1016/j.ejpb.2015.02.005>
- Hudait, A., Odendahl, N., Qiu, Y., Paesani, F., & Molinero, V. (2018). Ice-nucleating and antifreeze proteins recognize ice through a diversity of anchored clathrate and ice-like motifs. *Journal of the American Chemical Society*, *140*(14), 4905–4912. <https://doi.org/10.1021/jacs.8b01246>
- Inoue, T., Ebina, H., Dong, B., & Zheng, L. (2007). Electrical conductivity study on micelle formation of long-chain imidazolium ionic liquids in aqueous solution. *Journal of Colloid and Interface Science*, *314*(1), 236–241. <https://doi.org/10.1016/j.jcis.2007.05.052>

- IPCC. (2013). *Climate Change 2013: The Physical Science Basis. Contribution of Working Group I to the Fifth Assessment Report of the Intergovernmental Panel on Climate Change*. (T. Stocker, D. Qin, G.-K. Plattner, M. Tignor, S. Allen, J. Boschung, A. Nauels, Y. Xia, V. Bex, & P. Midgley, Eds.). Cambridge, United Kingdom and New York, NY, USA, Cambridge University Press.
- IUPAC. (1997). *Compendium of Chemical Terminology, 2nd ed (the "Gold Book")* (Second). Oxford, Blackwell Scientific Publications.
- Jover, A., Meijide, F., Rodríguez Núñez, E., Vázquez Tato, J., Mosquera, M., & Rodríguez Prieto, F. (1996). Unusual pyrene excimer formation during sodium deoxycholate gelation. *Langmuir*, *12*(7), 1789–1793. <https://doi.org/10.1021/la9506335>
- Kalyanasundaram, K. (1988). Pyrene fluorescence as a probe of fluorocarbon micelles and their mixed micelles with hydrocarbon surfactants. *Langmuir*, *4*(4), 942–945. <https://doi.org/10.1021/la00082a027>
- Kalyanasundaram, K., & Thomas, J. K. (1977). Environmental effects on vibronic band intensities in pyrene monomer fluorescence and their application in studies of micellar systems. *J. Am. Chem. Soc.*, *99*(7), 2039–2044. <https://doi.org/10.1021/ja00449a004>
- Kanji, Z. A., Ladino, L. A., Wex, H., Boose, Y., Burkert-Kohn, M., Cziczo, D. J., & Krämer, M. (2017). Overview of ice nucleating particles. *Meteorological Monographs*, *58*, 1.1–1.33. <https://doi.org/10.1175/AMSMONOGRAPHS-D-16-0006.1>
- Kawahigashi, M., & Fujitake, N. (1998). Surface-active properties of particle size fractions in two humic acids. *Soil Science and Plant Nutrition*, *44*(4), 497–505. <https://doi.org/10.1080/00380768.1998.10414473>
- Kim, H.-U., & Lim, K.-H. (2004). A model on the temperature dependence of critical micelle concentration. *Colloids and Surfaces A: Physicochemical and Engineering Aspects*, *235*(1), 121–128. <https://doi.org/10.1016/j.colsurfa.2003.12.019>
- Kiss, G., Tombácz, E., & Hansson, H.-C. (2005). Surface tension effects of humic-like substances in the aqueous extract of tropospheric fine aerosol. *J Atmos Chem*, *50*(3), 279–294. <https://doi.org/10.1007/s10874-005-5079-5>
- Knackstedt, K. A., Moffett, B. F., Hartmann, S., Wex, H., Hill, T. C. J., Glasgo, E. D., Reitz, L. A., Augustin-Bauditz, S., Beall, B. F. N., Bullerjahn, G. S., Fröhlich-Nowoisky, J., Grawe, S., Lubitz, J., Stratmann, F., & McKay, R. M. L. (2018). Terrestrial origin for abundant riverine nanoscale ice-nucleating particles. *Environmental Science & Technology*. <https://doi.org/10.1021/acs.est.8b03881>
- Kogej, K., & Škerjanc, J. (1999). Fluorescence and conductivity studies of polyelectrolyte-induced aggregation of alkyltrimethylammonium bromides. *Langmuir*, *15*(12), 4251–4258. <https://doi.org/10.1021/la9811517>
- Krofič, A., Frka, S., Simmel, M., Wex, H., & Grgić, I. (2018). Size-resolved surface-active substances of atmospheric aerosol: Reconsideration of the impact on cloud droplet formation. *Environ. Sci. Technol.*, *52*(16), 9179–9187. <https://doi.org/10.1021/acs.est.8b02381>
- Kumar, K., Patial, B. S., & Chauhan, S. (2015). Conductivity and fluorescence studies on the micellization properties of sodium cholate and sodium deoxycholate in aqueous medium at different temperatures: Effect of selected amino acids. *The Journal of Chemical Thermodynamics*, *82*, 25–33. <https://doi.org/10.1016/j.jct.2014.10.014>
- Kuwabara, C., Terauchi, R., Tochigi, H., Takaoka, H., Arakawa, K., & Fujikawa, S. (2014). Analysis of supercooling activities of surfactants. *Cryobiology*, *69*(1), 10–16. <https://doi.org/10.1016/j.cryobiol.2014.04.012>

- Latif, M. T., & Brimblecombe, P. (2004). Surfactants in atmospheric aerosols. *Environ. Sci. Technol.*, *38*(24), 6501–6506. <https://doi.org/10.1021/es049109n>
- Lauber, A., Kiselev, A., Pander, T., Handmann, P., & Leisner, T. (2018). Secondary ice formation during freezing of levitated droplets. *J. Atmos. Sci.* <https://doi.org/10.1175/JAS-D-18-0052.1>
- Li, M., Rharbi, Y., Huang, X., & Winnik, M. A. (2000). Small variations in the composition and properties of Triton X-100. *Journal of Colloid and Interface Science*, *230*(1), 135–139. <https://doi.org/10.1006/jcis.2000.7050>
- Lin, J. J., Kristensen, T. B., Calderón, S. M., Malila, J., & Prisle, N. L. (2020). Effects of surface tension time-evolution for CCN activation of a complex organic surfactant. *Environ. Sci.: Processes Impacts*, *22*(2), 271–284. <https://doi.org/10.1039/C9EM00426B>
- Maki, L. R., Galyan, E. L., Chang-Chien, M.-M., & Caldwell, D. R. (1974). Ice nucleation induced by *Pseudomonas syringae*. *Appl. Environ. Microbiol.*, *28*(3), 456–459.
- Malvern Instruments. (2013). Zetasizer Nano Series User Manual. Malvern Instruments.
- Malvern Instruments. (2020). Zetasizer Nano Series Brochure. Malvern Panalytical.
- Malvern Panalytical. (2020). Technical Note: Intensity - Volume - Number - Which size is correct?
- Marcolongo, J. P., & Miranda, M. (2011). Thermodynamics of sodium dodecyl sulfate (SDS) micellization: An undergraduate laboratory experiment. *J. Chem. Educ.*, *88*(5), 629–633. <https://doi.org/10.1021/ed900019u>
- Matsuoka, K., & Moroi, Y. (2002). Micelle formation of sodium deoxycholate and sodium ursodeoxycholate (Part 1). *Biochimica et Biophysica Acta (BBA) - Molecular and Cell Biology of Lipids*, *1580*(2), 189–199. [https://doi.org/10.1016/S1388-1981\(01\)00203-7](https://doi.org/10.1016/S1388-1981(01)00203-7)
- Mignani, C., Creamean, J. M., Zimmermann, L., Alewell, C., & Conen, F. (2019). New type of evidence for secondary ice formation at around -15°C in mixed-phase clouds. *Atmospheric Chemistry and Physics*, *19*(2), 877–886. <https://doi.org/10.5194/acp-19-877-2019>
- Miller, A. J., Brennan, K. P., Mignani, C., Wieder, J., David, R. O., & Borduas-Dedekind, N. (2020). Development of the drop Freezing Ice Nuclei Counter (FINC), intercomparison of droplet freezing techniques, and use of soluble lignin as an atmospheric ice nucleation standard. *Atmospheric Measurement Techniques Discussions*, 1–27. <https://doi.org/10.5194/amt-2020-414>
- Mochizuki, K., Qiu, Y., & Molinero, V. (2017). Promotion of homogeneous ice nucleation by soluble molecules. *J. Am. Chem. Soc.*, *139*(47), 17003–17006. <https://doi.org/10.1021/jacs.7b09549>
- Moffett, B. F., Hill, T. C. J., & DeMott, P. J. (2018). Abundance of biological ice nucleating particles in the Mississippi and its major tributaries. *Atmosphere*, *9*(8), 307. <https://doi.org/10.3390/atmos9080307>
- Morris, C. E., Georgakopoulos, D. G., & Sands, D. C. (2004). Ice nucleation active bacteria and their potential role in precipitation. *Journal de Physique IV (Proceedings)*, *121*, 87–103. <https://doi.org/10.1051/jp4:2004121004>
- Mueller, G. M., Wolber, P. K., & Warren, G. J. (1990). Clustering of ice nucleation protein correlates with ice nucleation activity. *Cryobiology*, *27*(4), 416–422. [https://doi.org/10.1016/0011-2240\(90\)90018-Y](https://doi.org/10.1016/0011-2240(90)90018-Y)
- Mukerjee, P., & Mysels, K. J. (1971). Critical micelle concentrations of aqueous surfactant systems. United States Department of Commerce, National Bureau of Standards, Office of Standard Reference Data.
- Nesměrák, K., & Němcová, I. (2006). Determination of Critical Micelle Concentration by Electrochemical Means. *Analytical Letters*, *39*(6), 1023–1040. <https://doi.org/10.1080/00032710600620302>

- Noudeh, G. D., Housaindokht, M., & Bazzaz, B. S. F. (2007). The effect of temperature on thermodynamic parameters of micellization of some surfactants.pdf. *Journal of Applied Sciences*, 7(1), 47–52.
- Nozière, B., Baduel, C., & Jaffrezo, J.-L. (2014). The dynamic surface tension of atmospheric aerosol surfactants reveals new aspects of cloud activation. *Nature Communications*, 5(1), 3335. <https://doi.org/10.1038/ncomms4335>
- Ogawa, S., Koga, M., & Osanai, S. (2009). Anomalous ice nucleation behavior in aqueous polyvinyl alcohol solutions. *Chemical Physics Letters*, 480(1), 86–89. <https://doi.org/10.1016/j.cplett.2009.08.046>
- O’Sullivan, D., Murray, B. J., Ross, J. F., Whale, T. F., Price, H. C., Atkinson, J. D., Umo, N. S., & Webb, M. E. (2015). The relevance of nanoscale biological fragments for ice nucleation in clouds. *Scientific Reports*, 5(1). <https://doi.org/10.1038/srep08082>
- Ovadnevaite, J., Zuend, A., Laaksonen, A., Sanchez, K. J., Roberts, G., Ceburnis, D., Decesari, S., Rinaldi, M., Hodas, N., Facchini, M. C., Seinfeld, J. H., & O’ Dowd, C. (2017). Surface tension prevails over solute effect in organic-influenced cloud droplet activation. *Nature*, 546(7660), 637–641. <https://doi.org/10.1038/nature22806>
- Pan, B., Ghosh, S., & Xing, B. (2008). Dissolved organic matter conformation and its interaction with pyrene as affected by water chemistry and concentration. *Environ. Sci. Technol.*, 42(5), 1594–1599. <https://doi.org/10.1021/es702431m>
- Pérez-Rodríguez, M., Prieto, G., Rega, C., Varela, L. M., Sarmiento, F., & Mosquera, V. (1998). A comparative study of the determination of the critical micelle concentration by conductivity and dielectric constant measurements. *Langmuir*, 14(16), 4422–4426. <https://doi.org/10.1021/la980296a>
- Perger, T.-M., & Bešter-Rogač, M. (2007). Thermodynamics of micelle formation of alkyltrimethylammonium chlorides from high performance electric conductivity measurements. *Journal of Colloid and Interface Science*, 313(1), 288–295. <https://doi.org/10.1016/j.jcis.2007.04.043>
- Perkins, R. J., Vazquez de Vasquez, M. G., Beasley, E. E., Hill, T. C., Stone, E. A., Allen, H. C., & DeMott, P. J. (2020). Relating structure and ice nucleation of mixed surfactant systems relevant to sea spray aerosol. *J. Phys. Chem. A*, acs.jpca.0c05849. <https://doi.org/10.1021/acs.jpca.0c05849>
- Petters, S. S., & Petters, M. D. (2016). Surfactant effect on cloud condensation nuclei for two-component internally mixed aerosols. *Journal of Geophysical Research: Atmospheres*, 121(4), 1878–1895. <https://doi.org/10.1002/2015JD024090>
- Pfrang, C., Rastogi, K., Cabrera-Martinez, E. R., Seddon, A. M., Dicko, C., Labrador, A., Plivelic, T. S., Cowieson, N., & Squires, A. M. (2017). Complex three-dimensional self-assembly in proxies for atmospheric aerosols. *Nat Commun*, 8(1), 1724. <https://doi.org/10.1038/s41467-017-01918-1>
- Piccolo, A. (2001). The supramolecular structure of humic substances. *Soil Science*, 166(11), 810–832. <https://doi.org/10.1097/00010694-200111000-00007>
- Piñeiro, L., Novo, M., & Al-Soufi, W. (2015). Fluorescence emission of pyrene in surfactant solutions. *Advances in Colloid and Interface Science*, 215, 1–12. <https://doi.org/10.1016/j.cis.2014.10.010>
- Polen, M., Brubaker, T., Somers, J., & Sullivan, R. C. (2018). Cleaning up our water: Reducing interferences from nonhomogeneous freezing of “pure” water in droplet freezing assays of ice-nucleating particles. *Atmospheric Measurement Techniques*, 11(9), 5315–5334. <https://doi.org/10.5194/amt-11-5315-2018>
- Popovitz-Biro, R., Wang, J. L., Majewski, J., Shavit, E., Leiserowitz, L., & Lahav, M. (1994). Induced freezing of supercooled water into ice by self-assembled crystalline monolayers of amphiphilic alcohols at the air-water interface. *J. Am. Chem. Soc.*, 116(4), 1179–1191. <https://doi.org/10.1021/ja00083a003>

- Pummer, B. G., Bauer, H., Bernardi, J., Bleicher, S., & Grothe, H. (2012). Suspendable macromolecules are responsible for ice nucleation activity of birch and conifer pollen. *Atmos. Chem. Phys.*, *12*(5), 2541–2550. <https://doi.org/10.5194/acp-12-2541-2012>
- Pummer, B. G., Budke, C., Augustin-Bauditz, S., Niedermeier, D., Felgitsch, L., Kampf, C. J., Huber, R. G., Liedl, K. R., Loerting, T., Moschen, T., Schauerl, M., Tollinger, M., Morris, C. E., Wex, H., Grothe, H., Pöschl, U., Koop, T., & Fröhlich-Nowoisky, J. (2015). Ice nucleation by water-soluble macromolecules. *Atmospheric Chemistry and Physics*, *15*(8), 4077–4091. <https://doi.org/10.5194/acp-15-4077-2015>
- Qiu, Y., Hudait, A., & Molinero, V. (2019). How size and aggregation of ice-binding proteins control their ice nucleation efficiency. *J. Am. Chem. Soc.*, *141*(18), 7439–7452. <https://doi.org/10.1021/jacs.9b01854>
- Qiu, Y., Odendahl, N., Hudait, A., Mason, R., Bertram, A. K., Paesani, F., DeMott, P. J., & Molinero, V. (2017). Ice nucleation efficiency of hydroxylated organic surfaces is controlled by their structural fluctuations and mismatch to ice. *J. Am. Chem. Soc.*, *139*(8), 3052–3064. <https://doi.org/10.1021/jacs.6b12210>
- Reicher, N., Segev, L., & Rudich, Y. (2018). The Weizmann Supercooled Droplets Observation on a Microarray (WISDOM) and application for ambient dust. *Atmos. Meas. Tech.*, *11*(1), 233–248. <https://doi.org/10.5194/amt-11-233-2018>
- Riechers, B., Wittbracht, F., Hütten, A., & Koop, T. (2013). The homogeneous ice nucleation rate of water droplets produced in a microfluidic device and the role of temperature uncertainty. *Phys. Chem. Chem. Phys.*, *15*(16), 5873–5887. <https://doi.org/10.1039/C3CP42437E>
- Rosen, M. J., & Kunjappu, J. T. (2012). *Surfactants and Interfacial Phenomena* (Fourth). John Wiley & Sons.
- Sareen, N., Schwier, A. N., Lathem, T. L., Nenes, A., & McNeill, V. F. (2013). Surfactants from the gas phase may promote cloud droplet formation. *Proceedings of the National Academy of Sciences*, *110*(8), 2723–2728. <https://doi.org/10.1073/pnas.1204838110>
- Schmid, D., Pridmore, D., Capitani, G., Battistutta, R., Neeser, J.-R., & Jann, A. (1997). Molecular organisation of the ice nucleation protein InaV from *Pseudomonas syringae*. *FEBS Letters*, *414*(3), 590–594. [https://doi.org/10.1016/S0014-5793\(97\)01079-X](https://doi.org/10.1016/S0014-5793(97)01079-X)
- Seinfeld, J. H., & Pandis, S. N. (2006). *Atmospheric chemistry and physics: From air pollution to climate change* (2nd ed). Hoboken, N.J, J. Wiley.
- Shah, S. S., Jamroz, N. U., & Sharif, Q. M. (2001). Micellization parameters and electrostatic interactions in micellar solution of sodium dodecyl sulfate (SDS) at different temperatures. *Colloids and Surfaces A: Physicochemical and Engineering Aspects*, *178*(1), 199–206. [https://doi.org/10.1016/S0927-7757\(00\)00697-X](https://doi.org/10.1016/S0927-7757(00)00697-X)
- Stan, C. A., Schneider, G. F., Shevkoplyas, S. S., Hashimoto, M., Ibanescu, M., Wiley, B. J., & Whitesides, G. M. (2009). A microfluidic apparatus for the study of ice nucleation in supercooled water drops. *Lab Chip*, *9*(16), 2293–2305. <https://doi.org/10.1039/B906198C>
- Steinke, I., Hiranuma, N., Funk, R., Höhler, K., Tüllmann, N., Umo, N. S., Weidler, P. G., Möhler, O., & Leisner, T. (2019). Complex plant-derived organic aerosol as ice-nucleating particles - more than a sum of their parts? *Atmos. Chem. Phys. Discuss.*, 1–17. <https://doi.org/10.5194/acp-2019-869>
- Storelvmo, T. (2017). Aerosol effects on climate via mixed-phase and ice clouds. *Annu. Rev. Earth Planet. Sci.*, *45*(1), 199–222. <https://doi.org/10.1146/annurev-earth-060115-012240>
- Streletsky, K., & Phillies, G. D. J. (1995). Temperature dependence of triton X-100 micelle size and hydration. *Langmuir*, *11*(1), 42–47. <https://doi.org/10.1021/la00001a011>

- Sugo, T., Okochi, H., Uchiyama, R., Yamanokoshi, E., Ogata, H., Katsumi, N., & Nakano, T. (2019). The role of humic-like substances as atmospheric surfactants in the formation of summer-heavy rainfall in downtown Tokyo. *City and Environment Interactions*, 3, 100022. <https://doi.org/10.1016/j.cacint.2020.100022>
- Sugo, T., Okochi, H., Uchiyama, R., Yamanokoshi, E., Ogata, H., Katsumi, N., & Nakano, T. (2020). The role of humic-like substances as atmospheric surfactants in the formation of summer-heavy rainfall in downtown Tokyo. *City and Environment Interactions*, 3, 100022. <https://doi.org/10.1016/j.cacint.2020.100022>
- Suski, K. J., Hill, T. C. J., Levin, E. J. T., Miller, A., DeMott, P. J., & Kreidenweis, S. M. (2018). Agricultural harvesting emissions of ice nucleating particles. *Atmospheric Chemistry and Physics Discussions*, 1–30. <https://doi.org/10.5194/acp-2018-348>
- Swift, R. S. (1999). Macromolecular properties of soil humic substances: Fact, fiction, and opinion. *Soil Science*, 164(11), 790–802.
- Tabazadeh, A. (2005). Organic aggregate formation in aerosols and its impact on the physicochemical properties of atmospheric particles. *Atmospheric Environment*, 39(30), 5472–5480. <https://doi.org/10.1016/j.atmosenv.2005.05.045>
- Taraniuk, I., Graber, E. R., Kostinski, A., & Rudich, Y. (2007). Surfactant properties of atmospheric and model humic-like substances (HULIS). *Geophysical Research Letters*, 34(16). <https://doi.org/10.1029/2007GL029576>
- Tarn, M. D., Sikora, S. N. F., Porter, G. C. E., O’Sullivan, D., Adams, M., Whale, T. F., Harrison, A. D., Vergara-Temprado, J., Wilson, T. W., Shim, J.-u., & Murray, B. J. (2018). The study of atmospheric ice-nucleating particles via microfluidically generated droplets. *Microfluid Nanofluid*, 22(5), 52. <https://doi.org/10.1007/s10404-018-2069-x>
- Tennouga, L., Mansri, A., Medjahed, K., Chetouani, A., & Warad, I. (2015). The micelle formation of cationic and anionic surfactants in aqueous medium: Determination of CMC and thermodynamic parameters at different temperatures. *J. Mater. Environ. Sci.*, 6(10), 2711–2716.
- Thakkar, K., Bharatiya, B., Shah, D. O., Ray, D., Aswal, V. K., & Bahadur, P. (2015). Interaction of ionic liquid type cationic surfactants with triton X-100 nonionic micelles. *Colloids and Surfaces A: Physicochemical and Engineering Aspects*, 484, 547–557. <https://doi.org/10.1016/j.colsurfa.2015.08.039>
- Topel, Ö., Çakır, B. A., Budama, L., & Hoda, N. (2013). Determination of critical micelle concentration of polybutadiene-block-poly(ethyleneoxide) diblock copolymer by fluorescence spectroscopy and dynamic light scattering. *Journal of Molecular Liquids*, 177, 40–43. <https://doi.org/10.1016/j.molliq.2012.10.013>
- Tuckermann, R. (2007). Surface tension of aqueous solutions of water-soluble organic and inorganic compounds. *Atmospheric Environment*, 11.
- Vali, G. (2019). Revisiting the differential freezing nucleus spectra derived from drop-freezing experiments: Methods of calculation, applications, and confidence limits. *Atmos. Meas. Tech.*, 12(2), 1219–1231. <https://doi.org/10.5194/amt-12-1219-2019>
- von Wandruszka, R. (1998). The micellar model of humic acid: Evidence from pyrene fluorescence measurements. *Soil Science*, 163(12), 921–930.
- Wang, G.-Y., Wang, Y.-Y., & Wang, X.-H. (2017). Aggregation behaviors of mixed systems for imidazole based ionic liquid surfactant and Triton X-100. *Journal of Molecular Liquids*, 232, 55–61. <https://doi.org/10.1016/j.molliq.2017.02.044>

- Wang, P. K. (2013). *Physics and Dynamics of Clouds and Precipitation*. Cambridge, Cambridge University Press. <https://doi.org/10.1017/CBO9780511794285>
- Wershaw, R. L. (1999). Molecular aggregation of humic substances. *Soil Science*, *164*(11), 803–813.
- Wilson, P. W., Osterday, K. E., Heneghan, A. F., & Haymet, A. D. J. (2010). Type I antifreeze proteins enhance ice nucleation above certain concentrations. *J. Biol. Chem.*, *285*(45), 34741–34745. <https://doi.org/10.1074/jbc.M110.171983>
- Wilson, T. W., Ladino, L. A., Alpert, P. A., Breckels, M. N., Brooks, I. M., Browse, J., Burrows, S. M., Carslaw, K. S., Huffman, J. A., Judd, C., Kilhau, W. P., Mason, R. H., McFiggans, G., Miller, L. A., Nájera, J. J., Polishchuk, E., Rae, S., Schiller, C. L., Si, M., ... Murray, B. J. (2015). A marine biogenic source of atmospheric ice-nucleating particles. *Nature*, *525*(7568), 234–238. <https://doi.org/10.1038/nature14986>
- Xue, H., Lu, Y., Geng, H., Dong, B., Wu, S., Fan, Q., Zhang, Z., Li, X., Zhou, X., & Wang, J. (2019). Hydroxyl groups on the graphene surfaces facilitate ice nucleation. *J. Phys. Chem. Lett.*, *10*(10), 2458–2462. <https://doi.org/10.1021/acs.jpcllett.9b01033>
- Zala, S. (2020). *Singlet oxygen indoors: Production rates and quantum yield measurements for indoor light sources and indoor air* (Master Thesis). ETH Zurich. Zurich, Switzerland.
- Zana, R., Lévy, H., & Kwetkat, K. (1998). Mixed micellization of dimeric (gemini) surfactants and conventional surfactants. I. Mixtures of an anionic dimeric surfactant and of the nonionic surfactants C12E5 and C12E8. *Journal of Colloid and Interface Science*, *197*(2), 370–376. <https://doi.org/10.1006/jcis.1997.5248>
- Zhang, S., Gao, Y., Dong, B., & Zheng, L. (2010). Interaction between the added long-chain ionic liquid 1-dodecyl-3-methylimidazolium tetrafluoroborate and Triton X-100 in aqueous solutions. *Colloids and Surfaces A: Physicochemical and Engineering Aspects*, *372*(1-3), 182–189. <https://doi.org/10.1016/j.colsurfa.2010.10.011>

9 Appendix

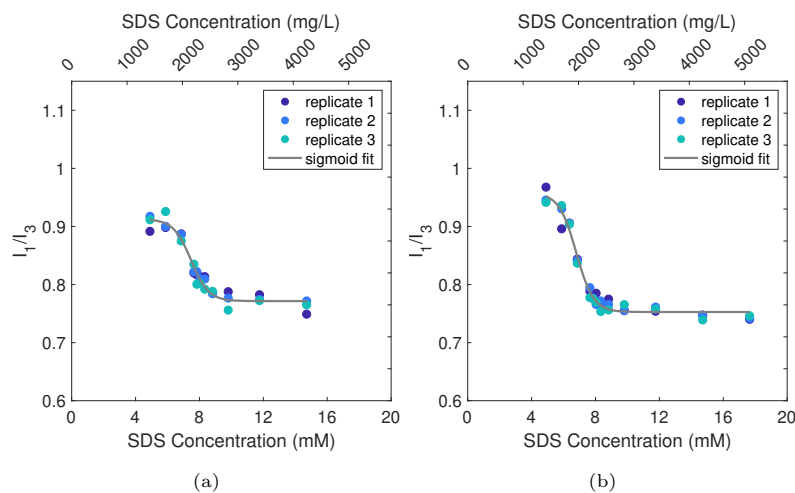


Figure A1: Pyrene fluorescence 1:3 ratio versus SDS concentration in two experiments (a) and (b). The I_1/I_3 ratio (y-axes) is the ratio of fluorescent intensities at 373 and 384 nm wavelengths. The markers indicate experimental values in triplicate at each concentration, and the curve is the sigmoid fit through the data. Replicates 1, 2, and 3 (dark to light blue) indicate results of identical solutions pipetted into three different wells. Samples at each concentration contain $2\ \mu\text{M}$ pyrene.

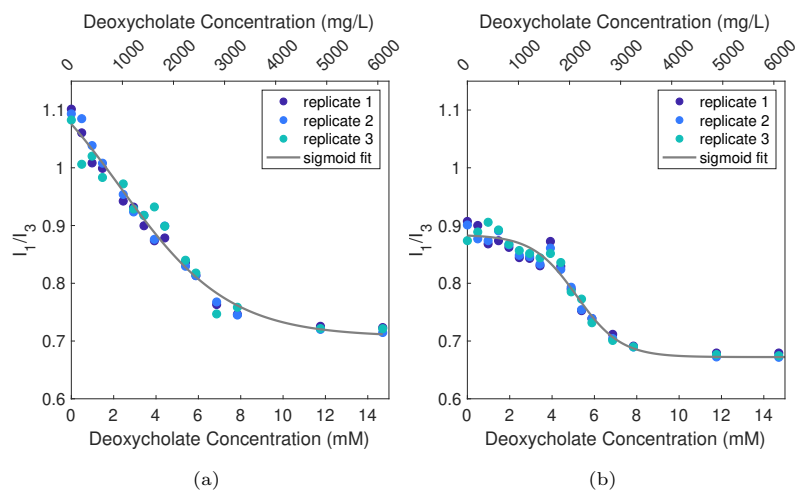


Figure A2: Pyrene fluorescence 1:3 ratio versus deoxycholate concentration in two experiments (a) and (b). The I_1/I_3 ratio (y-axes) is the ratio of fluorescent intensities at 373 and 384 nm wavelengths. The markers indicate experimental values in triplicate at each concentration, and the curve is the sigmoid fit through the data. Replicates 1, 2, and 3 (dark to light blue) indicate results of identical solutions pipetted into three different wells. Samples at each concentration contain $2\ \mu\text{M}$ pyrene.

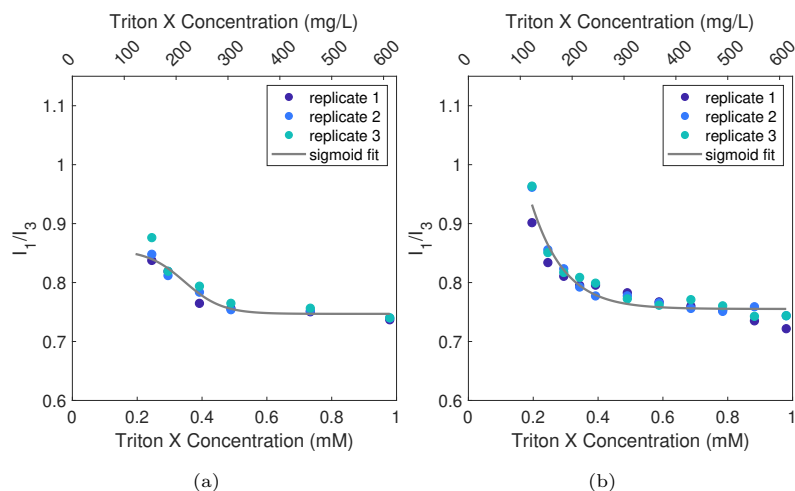


Figure A3: Pyrene fluorescence 1:3 ratio versus Triton X concentration in two experiments (a) and (b). The I_1/I_3 ratio (y-axes) is the ratio of fluorescent intensities at 373 and 384 nm wavelengths. The markers indicate experimental values in triplicate at each concentration, and the curve is the sigmoid fit through the data. Replicates 1, 2, and 3 (dark to light blue) indicate results of identical solutions pipetted into three different wells. Samples at each concentration contain $2 \mu\text{M}$ pyrene.

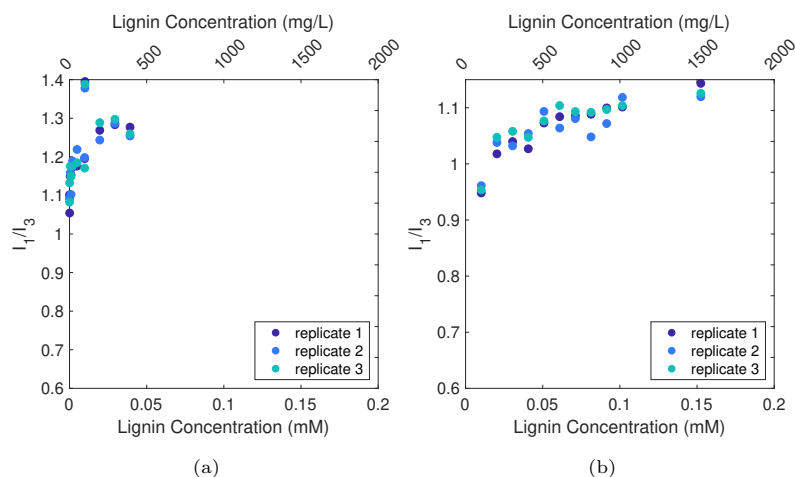


Figure A4: Pyrene fluorescence 1:3 ratio versus lignin concentration in two experiments (a) and (b). The I_1/I_3 ratio (y-axes) is the ratio of fluorescent intensities at 373 and 384 nm wavelengths. Replicates 1, 2, and 3 (dark to light blue) indicate results of identical solutions pipetted into three different wells. Samples at each concentration contain $2 \mu\text{M}$ pyrene.

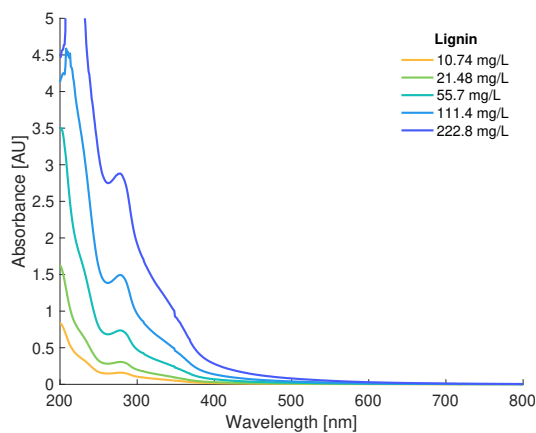


Figure A5: Absorbance of lignin from 200 to 800 nm at different concentrations (222.8, 111.4, 55.7, 21.48, 10.74 mg/L). Data provided by Zala (2020).

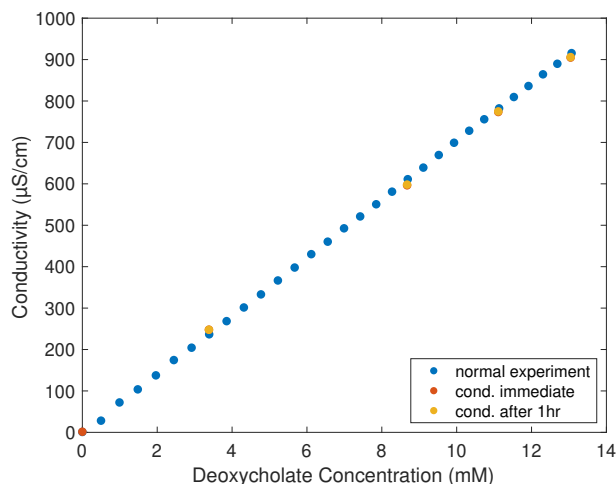


Figure A6: Results of the test of kinetics on deoxycholate micelle formation with conductivity. Conductivity was measured at 5 concentrations before (blue markers) and after (orange markers) one-hour resting time between each concentration range. Grey markers are the conductivity-concentration data from the prior normal experiment where conductivity was measured after only 2-5 minutes between concentration changes. Note that some markers (especially the red markers) may be hidden behind others because the values are so similar.

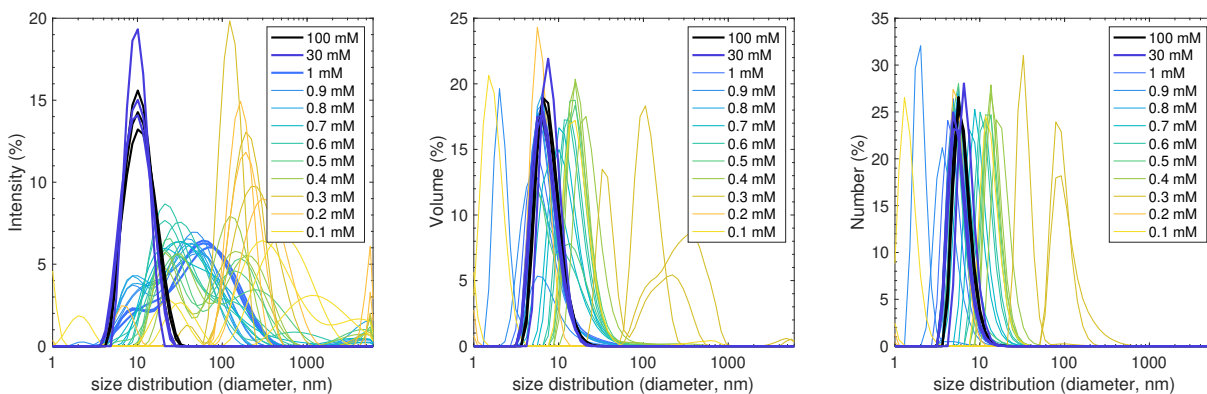


Figure A7: Size distributions for Triton X by percent intensity (left), percent volume (middle), and percent number (right) for all concentrations measured by DLS (dark blue to yellow with decreasing concentration from 100 mM to 0.1 mM).

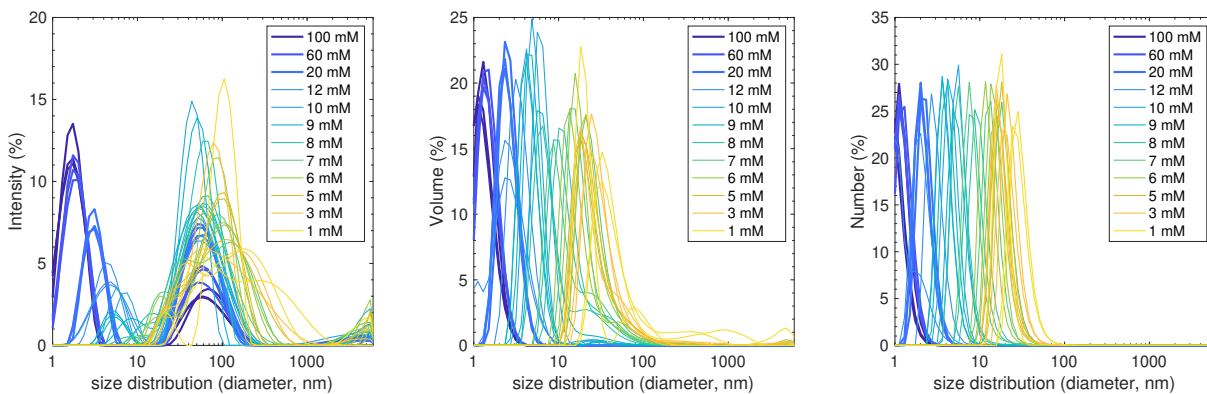


Figure A8: Size distributions for SDS by percent intensity (left), percent volume (middle), and percent number (right) for all concentrations measured by DLS (dark blue to yellow with decreasing concentration from 100 to 1 mM).

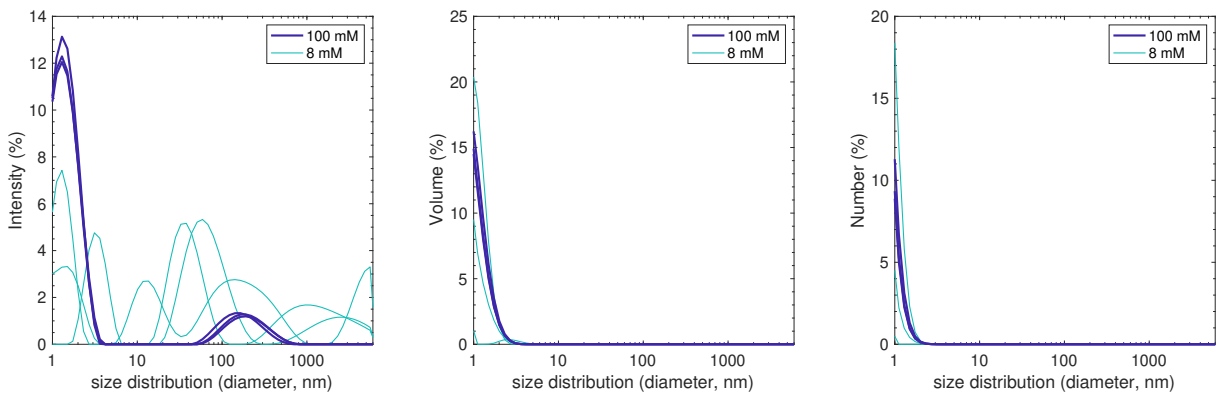


Figure A9: Size distributions for deoxycholate by percent intensity (left), percent volume (middle), and percent number (right) for all concentrations measured by DLS (dark blue for 100 mM and light blue for 8 mM).

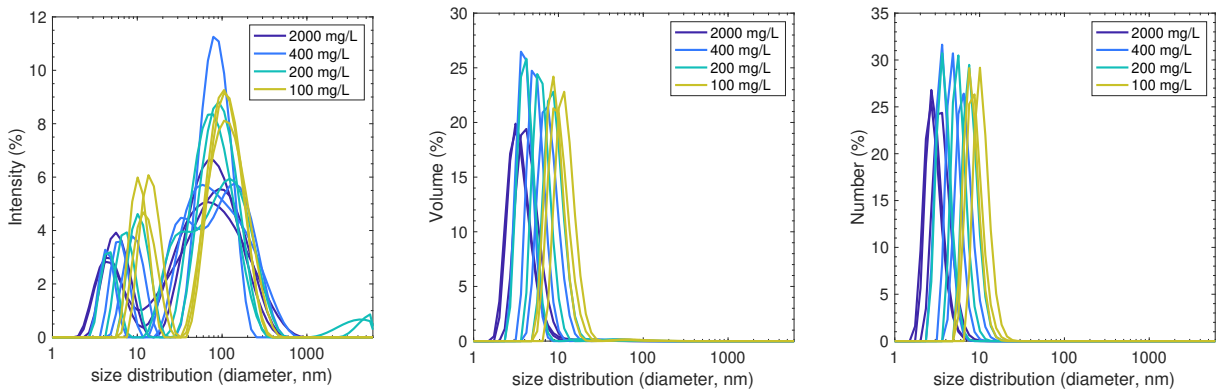


Figure A10: Size distributions for lignin by percent intensity (left), percent volume (middle), and percent number (right) for all concentrations measured on DLS (dark blue to yellow for decreasing concentration from 2000 to 100 mg/L).

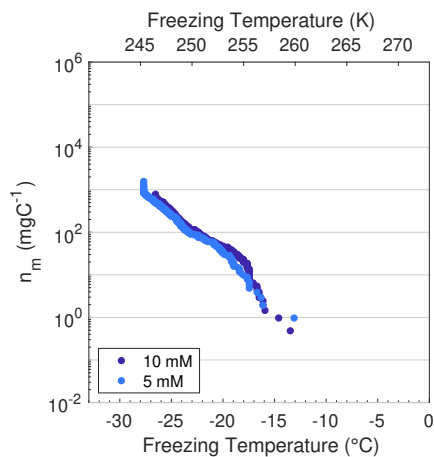


Figure A11: Ice-active mass site densities n_m versus temperature for two SDS concentrations of 10 and 5 mM.



Declaration of originality

The signed declaration of originality is a component of every semester paper, Bachelor's thesis, Master's thesis and any other degree paper undertaken during the course of studies, including the respective electronic versions.

Lecturers may also require a declaration of originality for other written papers compiled for their courses.

I hereby confirm that I am the sole author of the written work here enclosed and that I have compiled it in my own words. Parts excepted are corrections of form and content by the supervisor.

Title of work (in block letters):

Authored by (in block letters):

For papers written by groups the names of all authors are required.

Name(s):

First name(s):

.....
.....
.....
.....

With my signature I confirm that

- I have committed none of the forms of plagiarism described in the '[Citation etiquette](#)' information sheet.
- I have documented all methods, data and processes truthfully.
- I have not manipulated any data.
- I have mentioned all persons who were significant facilitators of the work.

I am aware that the work may be screened electronically for plagiarism.

Place, date

Signature(s)

.....	
.....
.....
.....

For papers written by groups the names of all authors are required. Their signatures collectively guarantee the entire content of the written paper.